NTNU
Norwegian University of
Science and Technology

AVO Analysis of the Upper Utsira Interface at the Sleipner Field during Fluid Substitution

Kjetil Roverud

Petroleum Geoscience and Engineering
Submission date: June 2017
Supervisor: Alexey Stovas, IGP

Norwegian University of Science and Technology
Department of Geoscience and Petroleum

Summary

Higher concentration of carbon dioxide (CO_2) in the atmosphere has contributed to increased interest in subsurface carbon capture and storage (CCS) projects. Geologic storage of CO_2 requires careful prior studies of geologic structures to prevent leakage. Further, repeated seismic surveys are required to monitor the evolution of the injected CO_2. This study performs a theoretical sensitivity analysis of the amplitude versus offset (AVO) coefficients to examine their correlations with CO_2 saturation. Also, the theoretical modeling is compared with seismic data to determine if the response post injection is detectable from seismic noise. The seismic data available is for a brine-filled formation. Different AVO methods are also evaluated in the thesis.

The area investigated in the study is the Sleipner field located in the middle of the Central North Sea. The field is a pioneer when it comes to CCS, where CO_2 is injected into the Utsira formation. The formation consists of mainly unconsolidated sand with an overburden shale layer. In this study, AVO analyses of the upper Utsira interface from well log data and seismic data are performed prior to injection. Then a reservoir model investigates the response during fluid substitution between brine water and CO_2.

The AVO response of the reservoir model is calculated using the Zoeppritz equation and the isotropic and anisotropic weak contrast approximation. The latter to determine the effect of including anisotropy in the AVO approximation. The result demonstrates that the effect is limited for the investigated interface. Further, the Zoeppritz equation and the isotropic approximation overlap for near offsets and diverge for far offsets. The effect of fluid substitution is well observed if the PP-wave reflection coefficient, R_{pp}, is plotted against the angle of incidence, θ. The trend is that the reflection coefficient becomes more negative as CO_2 substitutes brine water in the Utsira formation.

Trends are also observed crossplotting the AVO terms; the intercept (R_0), the gradient (G) and the curvature (K), respectively. The results show that the curvature term does not bring more valuable information as it is less sensitive to fluid substitution than the intercept and gradient terms. Crossplotting the intercept and gradient show that both terms decay strongly as CO_2 is injected into the Utsira formation. Further, a loss of sensitivity is observed as the CO_2

saturation increases. The result is that accurate determination of CO_2 content for high saturations are challenging.

Lastly, the response from the reservoir model is superimposed to the AVO response for a brine-filled Utsira formation from seismic data. The response from the seismic data is the extracted upper Utsira interface from two seismic sections. The effect for both sections is that the quantitatively theoretical AVO response for a CO_2 saturated formation generates a separate cluster away from the seismic response. This despite noise in the sections. The results show that the AVO method, in the area investigated, is sensitive to fluid substitution. The approach presented is expected to be applicable and valuable for CCS projects in the future.

Sammendrag

Økt konsentrasjon av karbondioksid (CO_2) i atmosfæren har ført til stadig større interesse for karbonfangst og –lagring i undergrunnen. For å kunne lagre CO_2 i geologiske formasjoner kreves en nøyaktig forhåndsanalyse. Dette for å forstå hvordan fluidet reagerer med formasjonen. Dersom CO_2 blir injisert i en geologisk formasjon kreves det gjentatte seismiske undersøkelser. Dette for å kontrollere at migrasjonen er som forventet og lekkasjer ikke forekommer. Dette studiet utfører en teoretisk sensitivitetsanalyse på den offset-avhengige amplituden (AVO). Hovedsakelig for å studere hvordan amplitudene endres med økt CO_2 metning. Videre, er den teoretiske responsen sammenlignet med responsen fra seismisk data for å bestemme om injeksjonen er observerbar med seismisk støy tilstedet.

Området utforsket er Sleipner feltet lokalisert sentralt i Nordsjøen. Feltet er ansett som en pioner for karbonfangst og –lagring, hvor CO_2 er injisert i Utsira formasjonen. Formasjonen består hovedsakelig av løs sandstein med en overliggende skifer. I studiet utføres AVO analyse på en brønnlogg og to seismiske seksjoner i området, samlet inn før injeksjonen av CO_2 startet. Videre, lages en reservoarmodell for å analysere AVO responsen når sjøvann erstattes av CO_2 i Utsira formasjonen.

AVO responsen analysert fra reservoarmodellen er kalkulert ved bruk av Zoeppritz likning, samt en isotropisk og anisotropisk lav-kontrasts approksimasjon. De to siste primært for å utforske verdien av å inkludere anisotropi i AVO likningene. Resultatet viser at verdien er minimal for overflaten analysert, hvor det med overflaten menes overgangen fra den overliggende skiferen til Utsira formasjonen. Zoeppritz likning og den isotropiske approksimasjonen viser samme resultat for nær vinkler, men differensierer seg for større vinkler. Effekten av injisert CO_2 er godt observert når refleksjonskoeffisienten, R_{pp}, er plottet mot innfallsvinkelen, θ. Den observerte trenden er at refleksjonskoeffisientene blir mer negative ettersom CO_2 substituerer sjøvannet i Utsira formasjonen.

Trendene observert i R_{pp} - θ plottene kan også observeres ved å plotte AVO koeffisientene R_0, G og K mot hverandre. Resultatene viser derimot at K leddet er minst sensitivt med hensyn til endring i fluidmetning. Derfor er størsteparten av analysen betraktet ved å plotte R_0 mot G.

Plottet viser at begge ledd synker kraftig for økt metning av CO_2 i Utsira formasjonen. Videre, blir sensitiviteten eller den relative forskjellen fra en metning til den neste mindre når metningen av CO_2 øker. Resultatet viser at en presis bestemmelse av CO_2 metning blir vanskelig når mengden sjøvann i reservoaret blir under halvparten av den totale metningen.

Responsen fra AVO analysen fra reservoarmodellen er plottet sammen med responsen fra en vannmettet Utsira formasjon fra seismisk data. Amplitudene som er hentet fra dataen er fra samme overflate som er studert fra reservoarmodellen. Responsen fra den seismiske dataen er utforsket for to seismiske seksjoner. Analysen fra begge seksjonene viser at den teoretiske AVO responsen for en delvis CO_2 mettet Utsira formasjon er synlig på AVO plottet selv med støy generert fra seismikken. Resultatet som fremlegges, for området analysert, viser at AVO metoden er sensitiv til injisering av CO_2. Metoden presentert er egnet for forhåndsanalyse for fremtidige karbonfangst og –lagrings prosjekter.

Preface

This study is the result of my Master Thesis completing my Master's degree in Petroleum Engineering at NTNU, with specialization in Geophysics. The report was written during the spring semester of 2017. The problem description and issues discussed were described and given by Professor Alexey Stovas.

I am very grateful to get the opportunity to study and analyze the AVO method. Further, I think carbon capture and storage projects are a relevant subject in present time. Mainly to decrease the emissions of carbon dioxide into our atmosphere.

The Master Thesis is written to an audience familiar with the petroleum industry. Further, knowledge in the field of geophysics is beneficial. This, as no geophysical background theory is presented. However, significant theory and equations are presented and explained.

Trondheim, June 11th, 2017.

Kjetil Roverud

Acknowledgement

I would like to thank my supervisor Professor Alexey Stovas for his guidance, expertise, and suggestions during the study. I could not have asked for a better supervisor.

I would also like to thank Professor Børge Arntsen and Associate Professor Kenneth Duffaut. Both contributing with data and valuable discussions and guidance. Data was also provided by the NTNU - NPD - SCHLUMBERGER PETREL READY Database, which I am truly grateful for. Also, I would like to thank the developers of the MatLab, Petrel and Promax software.

Finally, I would like to thank family and friends for the motivation given.

Table of Contents

List of Tables

List of Figures

Abbreviations

AVA	=	Amplitude Versus Angle
AVO	=	Amplitude Versus Offset
CCS	=	Carbon Capture and Storage
CIP	=	Common Image Point
CO_2	=	Carbon dioxide
G	=	Gradient
K	=	Curvature
P-wave	=	Pressure wave
R_0	=	Intercept
R_p	=	Pressure wave reflection coefficient
SRME	=	Surface Related Multiple Elimination
S-wave	=	Secondary wave
VTI	=	Vertical Transverse Isotropy

Chapter 1

Introduction

1.1 Background

The Sleipner field in the North Sea is a pioneer when it comes to carbon capture and storage (CCS). The process started in 1996 when carbon dioxide (CO_2), stripped from natural gas, was injected into the Utsira formation. Since then, over 10 million tons of CO_2 has been captured and stored in the structure. Today, many CCS projects are being developed worldwide to reduce the emission of CO_2. Before injections, a careful study of geological structures in the area is required to prevent gas leakage to the surface. On the Sleipner field, the CO_2 is stored in geologic layers within the Utsira formation and captured by overlying shale sequences.

An important factor regarding CCS is the need for reservoir monitoring. This to control the migration path of the CO_2 and make sure the evolution is as expected. Deviations from expected path might be an indication of leakage or changes in estimated rock properties. The most common way to monitor the subsurface exposed to CCS is by time-lapse seismic, also known as 4D seismic. Time-lapse seismic refers to repeated seismic surveys. In the Utsira formation, the method has successfully monitored the evolution of fluid substitution and the migration path of the CO_2.

There are many methods for comparison between datasets gathered pre-and post-injection. One method is referred to as amplitude variation with offset or amplitude versus offset (AVO). The method analyzes the amplitudes dependency with offset and is strongly sensitive to fluid substitution between brine water and a more compressible fluid, such as CO_2. This is confirmed in Brown et al. (2007) and Ravazzoli and Gómez (2011). Further, Eiken et al. (2000) advise

that the AVO method performed on the upper Utsira interface should track the areas exposed to fluid substitution. This conclusion is also reached by Ravazzoli and Gómez (2014). They demonstrate that a monotonic increase in magnitude for the reflection coefficient could be expected, with significant variations with respect to the pre-injection state. The AVO method itself is well discussed in literature (see [Ostrander (1984); Castagna and Swan (1997); Avseth et al. (2010)]).

Many authors have been investigating the changes in reflectivity due to injected CO_2 on time-lapse seismic images, among others Chadwick et al. (2004), Chadwick et al. (2009) and Furre and Eiken (2014). Further, Pan et al. (2016) combine time-lapse seismic and time-lapse AVO to monitor the CO_2 in the Utsira formation. Rabben and Ursin (2011) perform AVA inversion on the top Utsira formation. Additional emphasis, in the paper, is on how to pick and flatten the seismic gathers. Dupuy et al. (2016) present a synthetic study of AVO analysis applied to the Sleipner data.

1.2 Problem Definition and Approach

The first objective of this thesis is to analyze the AVO response of the upper Utsira interface during fluid substitution. This is done by generating a reservoir model and observe changes in the AVO response as CO_2 substitutes brine water. The results are important to determine the sensitivity of fluid substitution in the Utsira formation for AVO analysis. The second objective is to compare the modeled AVO response with the response from real seismic data. The seismic dataset used is prior to the injection and represents a brine-filled Utsira formation. Therefore, the AVO response is plotted together with the modeled response for different fluid saturations. This to observe in what degree the response is detectable from the noise present in the seismic gathers. The final objective is to evaluate the differences in the AVO response using different AVO methods. The methods used are the Zoeppritz equation and the isotropic and anisotropic weak contrast approximation. The software used is the MatLab, Petrel, and Promax software.

The sensitivity of the AVO method on fluid substitution is necessary for present and future CCS projects. The approach demonstrated in this thesis can be performed on future CCS projects before injection. This to bring valuable information for CO_2 monitoring problems. The report is motivated by investigating the AVO sensitivity during fluid substitution, and define the trends observed on real data.

The approach is to first determine the lithology and reservoir properties by investigating well log data in the area. Further, an AVO analysis is performed on the upper and lower Utsira interface from the well data. Rock parameters are then extracted from the well data and used to generate a reservoir model. Note that estimated parameters are used at depths where the well logs include high uncertainties. Further, fluid substitution in the sand layers of the reservoir model is performed. This by using the Gassmann equation. The effective medium properties of the reservoir model for different saturations is then calculated by Backus averaging. Then, the AVO response from the upper Utsira interface is calculated. Lastly, is the same interface extracted from the seismic sections. This to compare the modeled and true responses and observe if the fluid substitution is noticeable with seismic noise present.

The first chapter includes a general introduction of this study with problem definition and approach. The second chapter focuses on the geological settings in the area of interest. Further, the data used in this thesis is presented. The third chapter presents the theoretical framework. The chapter is modified from a project written prior to the thesis, written during the autumn semester of 2016 in *TPG4570*. Chapter 4 presents the research methodologies. The results and the discussion are presented in chapter 5 and 6, respectively. A summary with concluding remarks is given in chapter 7.

1.3 Limitations

The limitations of the approach are mainly related to the lack of well data available in the wells accessible at a depth of investigation. Also, did some of the original well logs require editing. Mainly because of washout and mud filtrate invasion. The effect can lead to errors in the estimated rock properties and the AVO modeling. For the AVO analysis particularly, appropriate P- and S-wave velocity logs would have been beneficial.

Another limitation is the restrictions regarding datasets available for the Sleipner area. For this thesis, only seismic data prior to injection of CO_2 was available. It would have been beneficial to compare the modeled AVO response after fluid substitution with real seismic data after injection also.

Chapter 2

Geological setting and data

2.1 Location and geology of storage site

The Sleipner field is located in the middle of the Central North Sea and embraces the Sleipner East and Sleipner West gas and condensate fields, illustrated in Figure 2.1. The gas produced from the Sleipner West field contains CO_2 which, due to environmental and economic reasons, is captured and injected into the subsurface (Furre and Eiken, 2014). The injection is done at the Sleipner East facility where the gas is stored in the Utsira formation.

The Utsira formation has a depth of approximately 800-1000 meters and a thickness of about 200-300 meters in the Sleipner area (Furre and Eiken, 2014). The formation comprises a basinally restricted deposit of Mio-Pliocene age extending for more than 400 kilometers from north to south and 50-100 kilometers from east to west (Chadwick et al., 2004). The formation consists of unconsolidated sands separated by thin intra-reservoir mudstones or shale layers. The sand layers are great reservoir rocks with a porosity of 35-40 percent and permeability in the order of several Darcys (Furre and Eiken, 2014). The intra-reservoir shale layers work as semi-permeable layers and are in general around one or two meters thick. In the Sleipner area, there is one exception, a thicker shale deposit in the upper Utsira formation of approximately five meters. The layer is located about 14 meters below the top of the Utsira formation.

The net to gross ratio (N/G) in the Utsira formation is on average 0.98, where net to gross ratio refers to the ratio of sand compared to shale. Hence, there is a fairly high ratio of sand present in the formation. The sand layers have a complex architecture with elongated sand bodies. The Utsira formation in the area of interest contains horizontal layers, and the upper

Utsira interface is easily detected both on well log data and seismic data. The lower Utsira interface is more difficult to track as it is more discontinuous.

The overlying cap rock is several hundred meters thick and is divided into three main sequences. The first sequence is approximately 50-100 meters. This is the shale layer investigated in this thesis. Primarily, because it is the initial sealing unit (Chadwick et al., 2004). Cutting samples from the sequence comprise dominantly massive gray silts or silty clays.

2.2 Well Log data

Four well logs are investigated in the study area, well 15/9-9, 15/9-11, 15/9-13 and 15/9-16. The location of the wells is shown in Figure 2.1. The complete well logs for each well can be found in Appendix B in Figure B.1 and B.2. Each well contains four logs; the caliper, gamma ray, sonic and density log. Well logs display characteristics of the subsurface in a borehole. This by using different tools to measure the physical properties of the rocks penetrated by the well (Bjorlykke, 2015). The quality of the interpretation depends highly on the condition of the borehole, mud used while drilling and the formation pressure. The well log data is presented to amplify and confirm the geologic settings introduced in Section 2.1. For a broader presentation of the well log tools see Rider (1996).

Figure 2.3 shows the original well logs from well 15/9-13 and well 15/9-11, at a depth of the Utsira formation. Note that the upper Utsira reflector or interface appears at nearly the same depth in both wells. This is also the case in the other two wells. This confirms a flat geology with horizontally layered formations at a depth of interest. The well logs are interpreted to investigate the properties of sand and shale sequences, respectively. For simplicity, the rest of the section focus on the observations detected from well 15/9-13. This as it is the well located closest to the seismic sections available. The background gas in the well, for the Utsira formation, is estimated to be $1 - 2\%$. This corresponds to an almost entirely brine saturated formation. Figure 2.2 shows the well path for the well. Note the vertical path to the depth of approximately 1500 meters. Implying that the properties measured at this depth are in the vertical direction.

The caliper tool, illustrated in track one in Figure 2.3, measures the size and shape of the borehole. If the borehole diameter has the same size as the drilling bit, it is called on gauge. This represents a good drilling performance but requires a well-consolidated formation. The

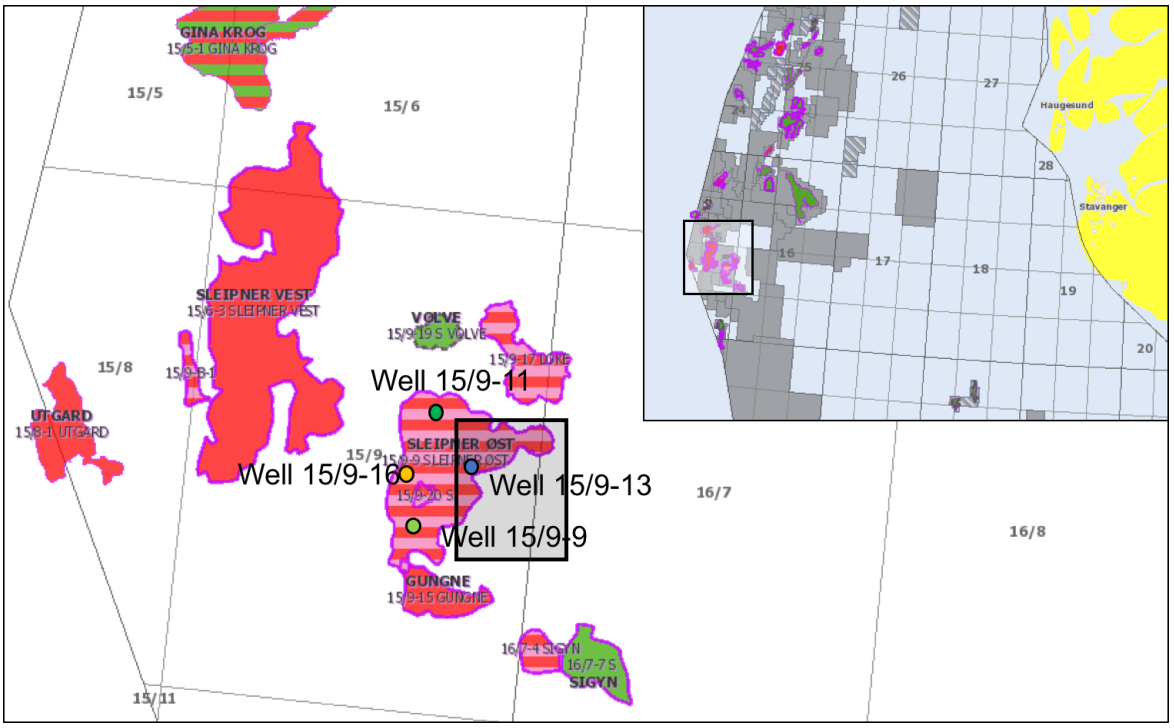

Figure 2.1: Map of the Sleipner area in the Central North Sea, west of Norway. The gray square shows the area covered by seismic used. The circles display the wells utilized in this study. Four wells are investigated, well 15/9-9, 15/9-11, 15/9-13 and 15/9-16.

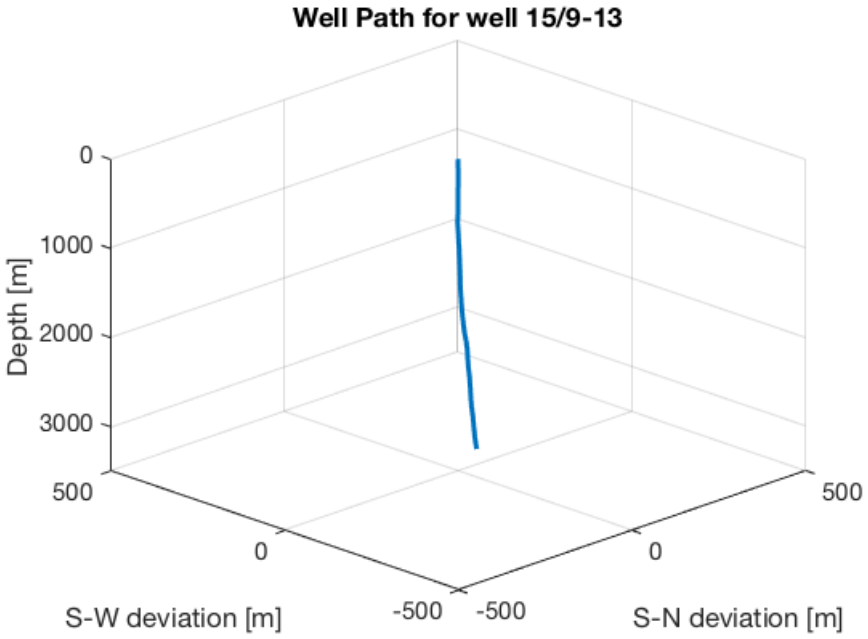

Figure 2.2: The vertical well path for well 15/9-13. Note that the well does not deviate before approximately 1500 meters.

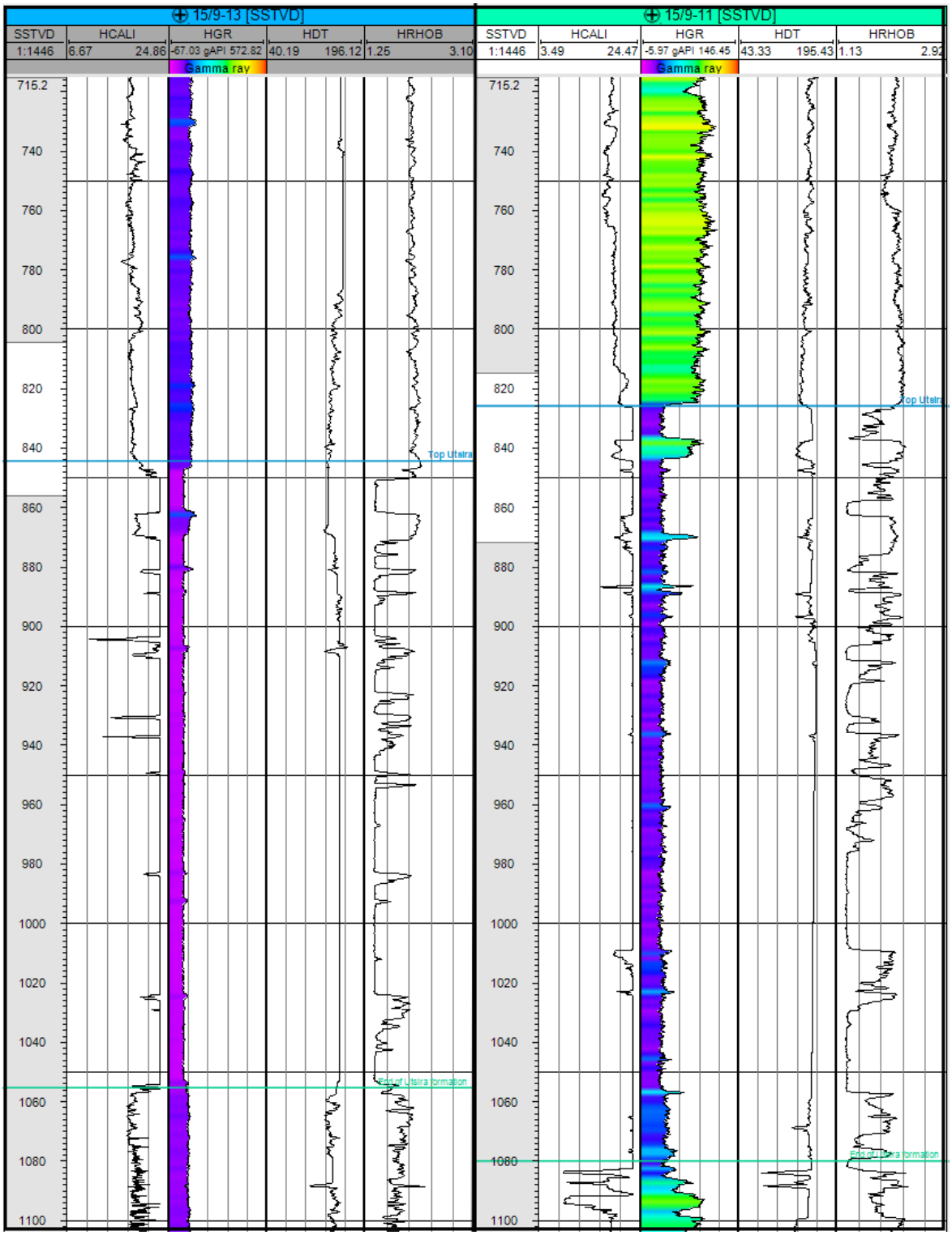

Figure 2.3: Well log data from well 15/9-13, to the left, and 15/9-11, to the right. The tracks display, from left to right, the caliper, gamma ray, sonic and density log. The blue line represents the upper Utsira interface and the green line the lower Utsira interface.

caliper readings are on gauge in the shale sequences in well 15/9-13, but not in the major parts of the Utsira formation. This confirms that the sand layers are unconsolidated and washes out in the borehole. The wash-outs generate more room for drilling mud which leads to mud filtrate invasion. It is understood that other tools, especially those with shallow investigation depth, tends to read mud properties instead of rock properties in these sections. Hence, the wash-out zones decrease the quality and reliability of the other well logs.

The sonic log is shown in track three in Figure 2.3. The log measures the interval transit time of a formation, denoted $\triangle t$. The transit time can be defined as a formations capacity to transmit seismic waves and is a measure of the slowness of the formation. From the well log one observes that the sonic log is constant through the Utsira formation although the other logs detect internal shale layers. There are reasons to believe that the readings in this interval are affected by the wash-out zones.

The overburden and the internal Utsira shale layers can easily be interpreted and identified by gamma ray and density log readings, illustrated in track two and four in Figure 2.3. The density log measures the bulk density, defined as the overall density of rock including the solid matrix and the fluid enclosed in the pores (Rider, 1996). The tool is dependent on the borehole condition, and the quality of the readings in the Utsira formation can be discussed. However, does it separate the sand and shale sequences and gives a good indication of lithology in cooperation with the gamma ray log. The shale sequences have detectable higher density and gamma ray readings. Internal shale layers are detected by gamma ray readings greater than 36 API.

2.3 Seismic data

In this study, a 1994 seismic dataset from the Sleipner area has been investigated. The dataset was acquired using five receiver cables towed at a depth of 8 meters (Raknes et al., 2015b). The cable length was 3000 meters with a cross line separation equal 100 meters. The dataset has been processed by the contractor and further by Raknes et al. (2015b). The processing steps performed by the contractor are listed in Table 2.1. Further processing steps by Raknes et al. (2015b) included a band pass filter and surface-related multiple elimination (SRME) before depth migration. In addition, was velocity models for the dataset generated.

Two seismic sections are investigated in this thesis. Both presented by common image point (CIP) angle gathers. The benefit of the sorting method is that it takes the dipping reflector

geometry into account. Imaged with a correct background velocity model will the events appear horizontal on the seismic angle gathers (Mahmoudian and Margrave, 2009). A gather can be defined as a collection of seismic traces which share a geometric attribute. The CIP-gathers are favorable for migration-based velocity analysis and AVO analysis. The latter as the angle domain makes it possible to extract information about the reflectivity as a function of angle. The assumptions made generating a CIP-gather may be violated if the geology is complex. However, the geology of the Utsira formation is estimated to be horizontal and simple. Note that the events in the gathers are representative for only one subsurface location.

The location of the seismic sections is shown in Figure 2.4. The sections are located in the same area with approximately 20 meters spacing. The distance to well 15/9-13 is approximately 800 meters. The sections will be referred to as Angline1 and Angline2. Both sections contain 320 gathers with 12.5 meters' space between each gather. Further, the gathers contain 40 traces with 2.5 degrees increment. Hence, reflection angles from $0-100$ degrees are covered. Leading to an incidence angle cover from $0-50$ degrees and an angle axis between –50 and 50 degrees. A common image point angle gather comparison for the respective sections is given in Appendix B in Figure B.3 and B.4. The seismic lines are shown in Figure B.5 and B.6. The location of the sections is almost equal, meaning that the same geology is present. Though, are two different velocity models used in the processing sequence. Angline1 is processed with a velocity model from the 1994 dataset, while Angline2 with a velocity model from the 2006 dataset. The location of the sections is outside the area exposed to CO_2 injection, and the velocity models are expected to be similar. However, some differences may occur affecting the curvature of the CIP-gathers.

The quality of the seismic image cube the sections are extracted from depends on the velocity models used and the processing performed by the contractor. The quality of the velocity models is discussed in Raknes et al. (2015a) and Raknes et al. (2015b). Regarding the processing performed by the contractor is the critical problem restricted offsets and reduction in recording length as wide angle data is removed from the dataset. The gathers are in general estimated to have a good quality, with some uncertainties regarding the high angle responses.

Table 2.1: Processing steps performed by the contractor.

	Processing steps performed by contractor
1	Restrict maximum offset to 1700 meters
2	Reduce recording length to 2.3s
3	Signature deconvolution and swell noise filter
4	Low cut filter (6Hz)
5	Sample time step to 2.0ms
6	Gain data (t^2 scaling factor)

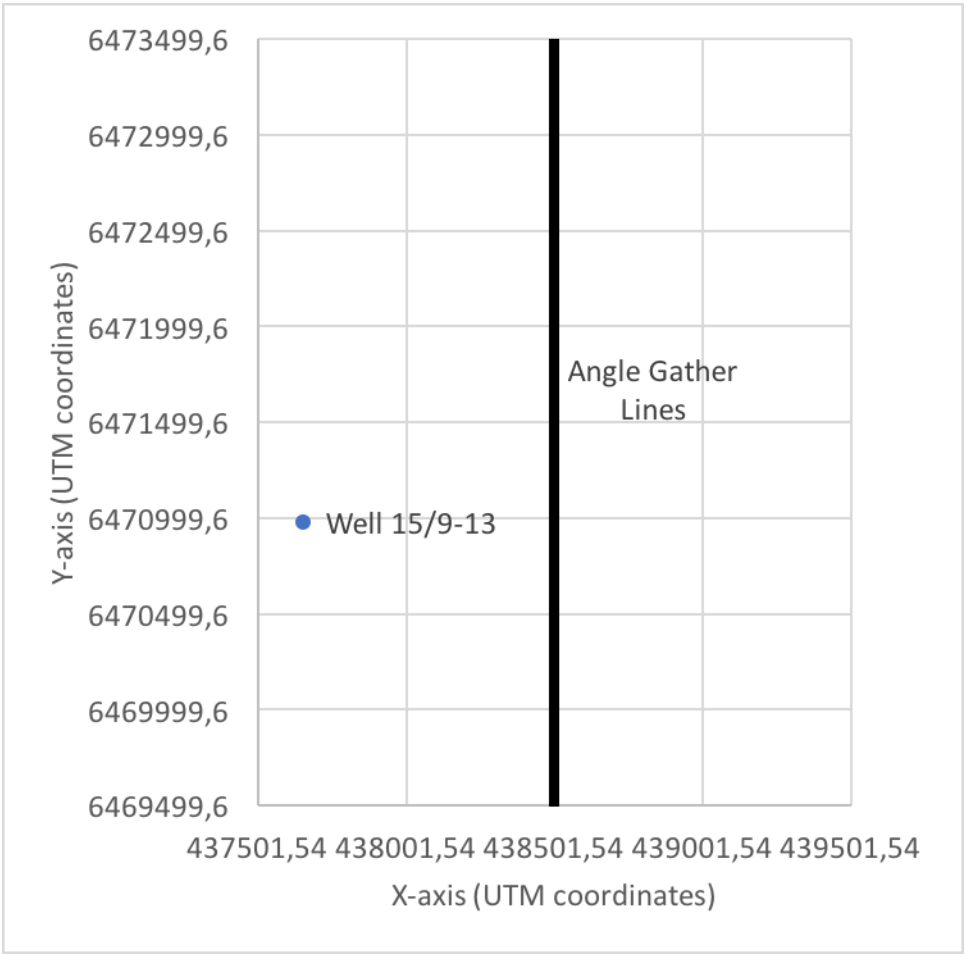

Figure 2.4: The location of the seismic sections used in this thesis, in addition to Well 15/9-13. The length of the seismic sections is 4 kilometers and the spacing between them 20 meters. The distance to well 15/9-13 is estimated to be 0.8 kilometers.

Chapter 3

Theoretical Framework

3.1 Gassmann Fluid Substitution

The seismic velocities control the seismic response in a reservoir. The P- and S-wave velocities in an elastic medium are given in equation 3.1 and 3.2.

$$V_p = \sqrt{\frac{K + \frac{4}{3}\mu}{\rho}}, \tag{3.1}$$

$$V_s = \sqrt{\frac{\mu}{\rho}}, \tag{3.2}$$

where μ is the shear modulus, K is the bulk modulus, and ρ is the bulk density of the medium. The elastic properties of the rock changes when performing the fluid substitution. The results are adjustments in the seismic response from the formation.

A common way to model the effect of fluid substitution is to use the Gassmann equation (Gassmann, 1951). The Gassmann equation makes it possible to compute both the P- and S-wave velocity and the density of a given formation for different fluid saturations. This by relating the saturated bulk modulus to porosity and the modulus of the pore fluid, rock frame, and matrix (Kumar, 2006). The Gassmann equation is presented in equation 3.3 and 3.4.

$$K_{sat} = K_{frame} + \frac{\left(1 - \frac{K_{frame}}{K_{matrix}}\right)^2}{\frac{\phi}{K_{fluid}} + \frac{(1-\phi)}{K_{matrix}} + \frac{K_{frame}}{K^2_{matrix}}}, \tag{3.3}$$

and

$$\mu_{dry} = \mu_{sat}, \tag{3.4}$$

where μ_{dry} and μ_{sat} are the dry and saturated shear modulus. K_{frame}, K_{matrix} and K_{fluid} are the bulk modulus of the rock frame, rock matrix, and pore fluid, respectively. For a brine water and carbon dioxide saturated medium, equation 3.5 can calculate the bulk modulus of the fluid. Note that the carbon dioxide is used as an example only and that the equations are applicable for other fluids to be substituted as well.

$$\frac{1}{K_{fluid}} = \frac{S_w}{K_{water}} + \frac{(1 - S_w)}{K_{CO_2}}, \tag{3.5}$$

where K_{water} is the bulk modulus of the brine water, K_{CO_2} is the bulk modulus of carbon dioxide and S_w is the water saturation. Equation 3.3 and 3.4 imply that an adjustment in pore fluid will alter the bulk modulus, but not the shear modulus. This is consistent with the argumentation in Berryman (1999). The Gassmann equation is applicable only when the water and gas phases are uniformly mixed at a very small scale (Avseth et al., 2010).

After performing the Gassmann equation, the P- and S-wave velocities can be reassembled for different saturations. To do so the initial bulk modulus in equation 3.1 is substituted with the saturated bulk modulus calculated in equation 3.3. The density for the given saturation can be calculated using equation 3.6 and 3.7.

$$\rho_{fluid} = (1 - S_w)\rho_{CO_2} + S_w\rho_{water}, \tag{3.6}$$

$$\rho_{sat} = (1 - \phi)\rho_{matrix} + \phi\rho_{fluid}, \tag{3.7}$$

where ρ_{matrix}, ρ_{water} and ρ_{CO_2} are the densities of the rock matrix, brine water, and carbon dioxide, respectively. Further, ρ_{sat} is the density of the saturated formation.

The Gassmann equation includes some fundamental assumptions where most of them are absent in a real-life reservoir. One of the assumptions is that the formation is completely isotropic. This is rarely the case. Other assumptions are low-frequency data, homogeneous mineralogy and a closed reservoir boundary. The limitations of the approach are further discussed in Avseth et al. (2010) and Collet and Gurevich (2013a).

3.2 Greenberg and Castagna for S-Wave Velocity Estimation

The S-wave velocity can be estimated from well log data by using the sonic log and the Greenberg and Castagna equation (Greenberg and Castagna, 1992). P-and S-wave velocities are critical parameters in geophysics and required to perform most seismic attributes, where seismic attributes are defined to be measurements based on seismic data (Herron, 2011). Understanding the P- and S-wave velocity help investigates rock and fluid properties and hence the seismic response.

The P-wave velocity can be calculated from the sonic log. A record of the measured S-wave velocity is though rarely available. However, the S-wave velocity is necessary for practical purposes such as in seismic modeling, AVO analysis and seismic applications (Eskandari et al., 2003). Greenberg and Castagna (1992) developed a general method for estimating the S-wave velocity from the P-wave velocity in porous rocks. The equation is given in equation 3.8.

$$
\begin{aligned}
V_s &= \frac{1}{2}\left\{\left[\sum_{i=1}^{L} X_i \sum_{j=0}^{N_i} a_{ij} V_P^j\right] + \left[\sum_{i=1}^{L} X_i \left(\sum_{j=0}^{N_i} a_{ij} V_p^j\right)^{-1}\right]^{-1}\right\}, \\
1 &= \sum_{i=0}^{L} X_i,
\end{aligned}
\tag{3.8}
$$

where L is the number of monomineralic porous constituents, X_i is the dry lithology volume fraction of lithological constituent i, a_{ij} are the empirical coefficients and $0 \leq N_i$ the order of polynomial i. Greenberg and Castagna (1992) tested and verified the method with laboratory measurements and full waveform sonic logs.

The Greenberg and Castagna equation calculates the shear-wave velocity by averaging the harmonic and arithmetic means of the constituent pure lithology shear velocities. One of the benefits of the method is that the P-wave velocity is the input rather than porosity. The success of the Greenberg and Castagna equation depends on: (1) the relationship between P- and S-wave velocities for water saturated, pure, porous lithologies; (2) nearly linear mixing laws for solid rock constituents; (3) first order applicability of the Biot-Gassmann theory to real rocks (Greenberg and Castagna, 1992). The prediction is dependent on the quality of the measured or calculated P-wave velocity. Therefore, a quality control of the P-wave velocity should be performed before using the equation.

The equation can be simplified in pure porous lithologies by using representative regression

Table 3.1: Regression coefficients for pure monomineralic lithologies.

Lithology	a_{i2}	a_{i1}	a_{i0}
Sandstone	0	0.80416	-0.85588
Limestone	-0.05508	1.01677	-1.03049
Dolomite	0	0.58321	-0.03049
Shale	0	0.76969	-0.86735

coefficients. The equation is given in equation 3.9.

$$V_s = a_{i2}V_p^2 + a_{i1}V_p + a_{i0}, \tag{3.9}$$

where a_{i2}, a_{i1} and a_{i0} represent the regression coefficients. The units of the P-and S-wave velocities are in km/s. The regression coefficients for the individual lithologies are given in Table 3.1. Note that the above equation is for water-saturated rocks. To measure the S-wave velocity from the P-wave velocity for other saturations one have to use Gassmann's equation in an iterative manner (Avseth et al., 2010).

3.3 Backus Averaging

Backus averaging is often used to upscale well log data to estimate the elastic properties of a stack of thin layers. The method transforms thinly layered mediums composed of either isotropic or anisotropic layers into one homogeneous anisotropic medium.

The upscaling approach generates anisotropy even though the thin layers themselves are isotropic, allowing us to estimate layer induced anisotropy analytically. The final anisotropy is then a function of heterogeneity, defined to be variation in properties upon position. This because it is the ordered heterogeneity on the small scale that creates the anisotropy on the larger scale (Thomsen, 2002). The elastic properties of the effective medium depend on the variation of properties in the sequence to be averaged (Berryman, 1999). Larger scale is defined as the longer seismic wavelengths compared to the thin layer thicknesses.

To perform Backus averaging one need a large seismic wavelength (λ) compared to the layer thickness (L), illustrated in Figure 3.1 (Backus, 1962). The ratio of the dominant wavelength to the typical layer thickness, λ/L, is broadly discussed in the literature, ranging from three to eleven. Stovas and Arntsen (2003) conclude that the critical ratio in the weak contrast limit is $\lambda/L = 4$. With weak contrast means a low reflectivity coefficient between the layers to

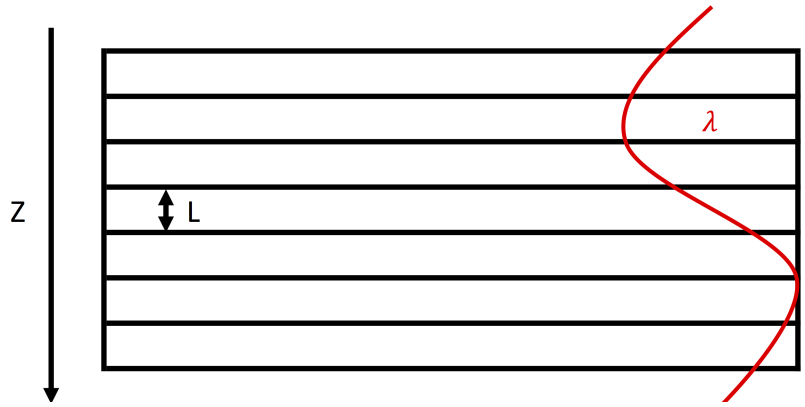

Figure 3.1: A stack of layers with layer thickness equal L. Note the large wavelength compared to L.

be averaged. Further, the minimum value for which the theory is valid tends to increase with increasing reflection coefficients (Stovas et al., 2006).

The elastic coefficients for each layer, j, are given by Thomsen (1986) notation in equation 3.10 and 3.11. Assuming isotropic and anisotropic layers, respectively.

$$\begin{aligned} c_{33,j} &= \rho_j V_{P,j}^2, \\ c_{44,j} &= \rho_j V_{S,j}^2, \\ c_{13,j} &= c_{33,j} - 2c_{44,j}, \\ c_{11,j} &= c_{33,j}, \end{aligned} \tag{3.10}$$

where $c_{33,j}$, $c_{44,j}$, $c_{13,j}$ and $c_{11,j}$ represent the elastic coefficients, ρ_j, $V_{P,j}^2$ and $V_{S,j}^2$ represent the density, P- and S-wave velocity of an individual layer, respectively.

$$\begin{aligned} c_{33,j} &= \rho_j V_{P,j}^2, \\ c_{44,j} &= \rho_j V_{S,j}^2, \\ c_{13,j} &= \sqrt{(c_{33,j} - c_{44,j})(c_{33,j}(1+2\delta_j) - c_{44,j})} - c_{44,j}, \\ c_{11,j} &= c_{33,j}(1+2\varepsilon_j), \end{aligned} \tag{3.11}$$

where δ_j and ε_j are the anisotropic parameters for the lithology. Note that for an isotropic medium there are only two independent elastic coefficients, $c_{33,j}$ and $c_{44,j}$. This is not the case for an anisotropic medium.

The analytical expressions for Backus averaging computing the effective elastic coefficients

are given by equation 3.12.

$$\begin{aligned}
\tilde{c}_{13} &= \langle c_{13}c_{33}^{-1}\rangle\langle c_{33}^{-1}\rangle^{-1}, \\
\tilde{c}_{11} &= \langle c_{11} - c_{13}^{2}c_{33}^{-1}\rangle + \langle c_{13}c_{33}^{-1}\rangle^{2}\langle c_{33}^{-1}\rangle^{-1}, \\
\tilde{c}_{33} &= \langle c_{33}^{-1}\rangle^{-1}, \\
\tilde{c}_{44} &= \langle c_{44}^{-1}\rangle^{-1}, \\
\tilde{c}_{66} &= \langle c_{66}\rangle,
\end{aligned} \tag{3.12}$$

where $\tilde{c}_{i,j}$ represents the elastic coefficients for the effective medium and $c_{i,j}$ the individual layer coefficients. Five non-zero coefficients describe the homogeneous anisotropic effective medium. The brackets in the equations represent the unweighted arithmetic average of layer properties given in equation 3.13.

$$\langle m_k \rangle = \frac{1}{N}\sum_{k=1}^{N} m_k. \tag{3.13}$$

The effective elastic coefficients are beneficial as they compute the effective medium properties and effective anisotropic parameters. The effective medium properties are given in equation 3.14 and 3.15.

$$\tilde{V}_{P0} = \sqrt{\frac{\tilde{c}_{33}}{\tilde{\rho}}}, \tag{3.14}$$

$$\tilde{V}_{S0} = \sqrt{\frac{\tilde{c}_{44}}{\tilde{\rho}}}, \tag{3.15}$$

where

$$\tilde{\rho} = \langle \rho \rangle. \tag{3.16}$$

Note that the velocities are equal the vertical velocities if the well is vertical and a vertical transverse isotropic (VTI) medium is assumed. A VTI medium has a vertical symmetry, with isotropic layers oriented horizontally. The effective anisotropic parameters are also calculated using Thomsen (1986) notation. The equations are given in equation 3.17.

$$\begin{aligned}\tilde{\epsilon} &= \frac{\tilde{c}_{11} - \tilde{c}_{33}}{2\tilde{c}_{33}},\\ \tilde{\delta} &= \frac{(\tilde{c}_{13} + \tilde{c}_{44})^2 - (\tilde{c}_{33} - \tilde{c}_{44})^2}{2\tilde{c}_{33}(\tilde{c}_{33} - \tilde{c}_{44})},\\ \tilde{\gamma} &= \frac{\tilde{c}_{66} - \tilde{c}_{44}}{2\tilde{c}_{44}},\end{aligned} \tag{3.17}$$

where $\tilde{\epsilon}$, $\tilde{\delta}$ and $\tilde{\gamma}$ represent the effective epsilon, delta and gamma parameters. The parameters describe the variation in P-and S-wave velocities as a function of polar angle with symmetry axis and are useful to quantify the degree of anisotropy (Collet and Gurevich, 2013b). The parameters have become the VTI anisotropies to analyze and characterize in anisotropic formations (Thomsen, 2002). For a layered isotropic medium will $\epsilon - \delta \geq 0$ (Berryman, 1997)

3.4 Amplitude Versus Offset

The reflection coefficient at an interface separating two mediums will vary with angle of incidence, illustrated in Figure 3.2. Amplitude versus offset or amplitude variation with offset (AVO) is the general term describing the amplitudes dependency with offset, or incidence angle. AVO is also known as amplitude variation with angle (AVA) because of the relationship between the angle of incidence and the reflection coefficient. However, since the offset determines the angle of incidence and the other way around, only the term AVO will be used in this thesis. Ostrander (1984) was the first to quantify the method by demonstrating the change in AVO response from a gas sand capped by a shale. The AVO technique is very popular in the oil industry as it makes it possible to explain seismic amplitudes regarding rock properties (Avseth et al., 2010). This by investigating the change in reflection coefficient by increasing the angle of incidence. A broader discussion about the history of AVO is presented in Castagna and Backus (1993).

3.4.1 Zoeppritz equation

For analysis of the PP-wave reflections, the Zoeppritz equation is used. A PP-wave reflection refers to the reflected P-wave from an incident P-wave at an interface. The equation assumes isotropic media and needs to be modified if anisotropy is present on either side of the interface investigated. The equation relates the amplitude of the incidence P-wave to the reflected

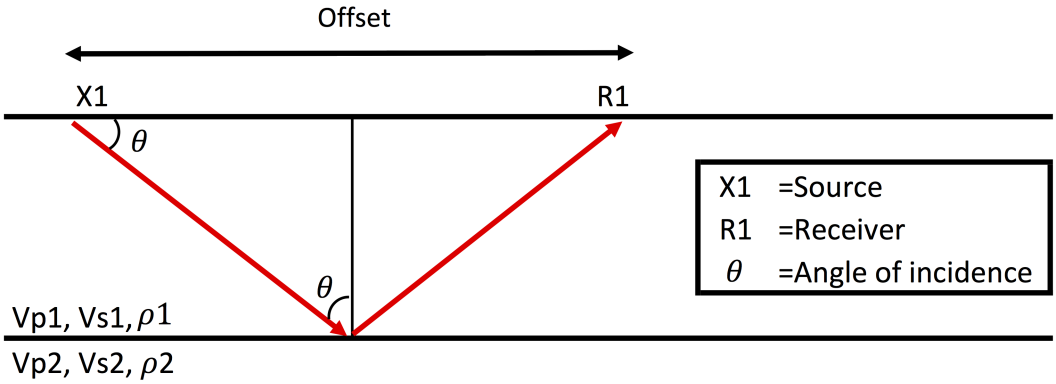

Figure 3.2: Diagram showing the layout of the source, receiver, and angle of incidence on the interface of interest.

and transmitted P- and S-waves for a given angle of incidence. The theory of the Zoeppritz equation is widely discussed in the literature and only necessary information to understand the equations and notations will be reproduced in this section. For the full theory of the equations see Zoeppritz (1919) and Aki and Richards (1980). The equation for the PP-wave reflection coefficient is given in equation 3.18. For simplicity is the P-and S-wave velocity denoted α and β, respectively.

$$\grave{P}\acute{P} = \left[\left(b\frac{cos(i_1)}{\alpha_1} - c\frac{cos(i_2)}{\alpha_2}\right)F - \left(a + d\frac{cos(i_1)}{\alpha_1}\frac{cos(j_2)}{\beta_2}\right)Hp^2\right]/D. \tag{3.18}$$

The equation is build up by several simple formulas shown in equation 3.19 and 3.20.

$$\begin{aligned} a &= \rho_2(1-2\beta_2^2p^2) - \rho_1(1-2\beta_1^2p^2), & b &= \rho_2(1-2\beta_2^2p^2) + 2\rho_1\beta_1^2p^2, \\ c &= \rho_1(1-2\beta_1^2p^2) + 2\rho_2\beta_2^2p^2, & d &= 2(\rho_2\beta_2^2 - \rho_1\beta_1^2), \end{aligned} \tag{3.19}$$

which lead to the cosine-dependent terms

$$\begin{aligned} E &= b\frac{cos(i_1)}{\alpha_1} + c\frac{cos(i_2)}{\alpha_2}, & F &= b\frac{cos(j_1)}{\beta_1} + c\frac{cos(j_2)}{\beta_2}, \\ G &= a - d\frac{cos(i_1)}{\alpha_1}\frac{cos(j_2)}{\beta_2}, & H &= a - d\frac{cos(i_2)}{\alpha_2}\frac{cos(j_1)}{\beta_1}, \\ D &= EF + GHp^2, \end{aligned} \tag{3.20}$$

where

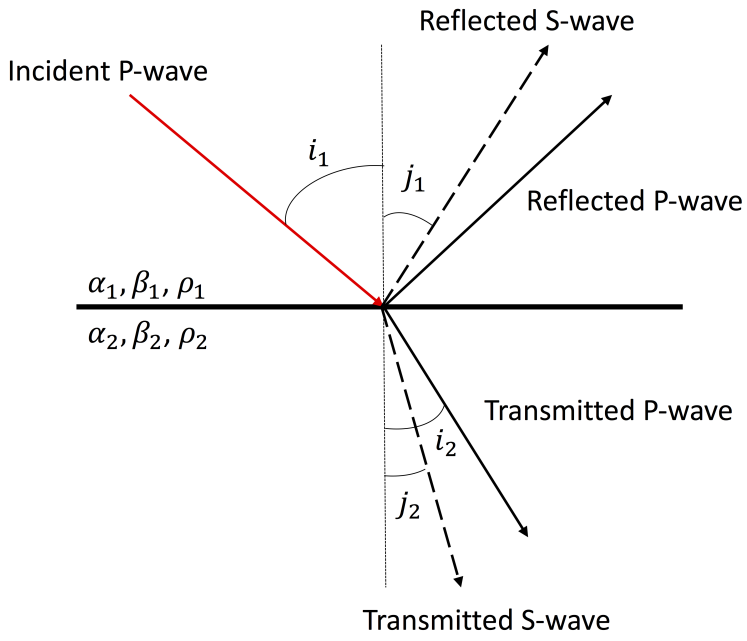

Figure 3.3: Schematic illustration of the parameters and angles used for the Zoeppritz equation.

$$p = \frac{sin(i_1)}{\alpha_1} = \frac{sin(i_2)}{\alpha_2} = \frac{sin(j_1)}{\beta_1} = \frac{sin(j_2)}{\beta_2}, \tag{3.21}$$

i_1, i_2, j_1 and j_2 represent the incident P, transmitted P, reflected S and transmitted S-wave angle, respectively. Further, α, β and ρ represent the velocities and density of a given formation. A schematic illustration is displayed in Figure 3.3. Note that the coherency in equation 3.21 comes from Snell's law.

3.4.2 Approximation of the Zoeppritz equation

The Zoeppritz equation is an exact calculation of the P-wave reflection coefficient but does not lead to an intuitive understanding of the AVO analysis. Therefore, several approximations to the equation are generated. The weak contrast approximation by Thomsen (2002) notation is given in equation 3.22 [see (Rüger, 2002; Banik, 1987)].

$$R_{pp} = R_0 + Gsin^2(\theta) + Ksin^2(\theta)tan^2(\theta), \tag{3.22}$$

where R_{pp} is the PP-wave reflection coefficient and θ the angle of incidence. R_0, G and K

represent the intercept, gradient and curvature given in equation 3.23, 3.24 and 3.25.

$$R_0 = \frac{1}{2}\left[\frac{\triangle V_{P0}}{\overline{V}_{P0}} + \frac{\triangle \rho}{\overline{\rho}}\right], \tag{3.23}$$

$$G = \frac{1}{2}\left[\frac{\triangle V_{P0}}{\overline{V}_{P0}} - \frac{4\overline{V}_{S0}^2}{\overline{V}_{P0}^2}\left(\frac{\triangle \rho}{\overline{\rho}} + \frac{2 \triangle V_{S0}}{\overline{V}_{S0}}\right) + \triangle \delta\right], \tag{3.24}$$

$$K = \frac{1}{2}\left[\frac{\triangle V_{P0}}{\overline{V}_{P0}} + \triangle \epsilon\right], \tag{3.25}$$

where $\triangle V_{P0}$, $\triangle V_{S0}$, $\triangle \rho$, $\triangle \delta$ and $\triangle \epsilon$ represent the changes in V_{P0}, V_{S0}, ρ, δ and ϵ over an interface. The changes are calculated by subtracting the properties from the underlying medium from the overlying. Further, $\overline{V}_{P0}$, $\overline{V}_{S0}$, and $\overline{\rho}$ represents the averaged properties over the same interface. Note that the velocities are vertical velocities. The equations include the effective jump in anisotropic parameters and take anisotropy into account. The isotropic approximation is given by setting $\triangle \delta$ and $\triangle \epsilon$ equal zero.

R_0, G and K are interface properties meaning that they are a function of changed physical properties over an interface (Thomsen, 2002). R_0 describes the normal incidence reflection, meaning the angle of incidence at zero degrees (zero offsets). G and K represent the gradient at intermediate and far offsets, respectively. The AVO coefficients can be used to identify lithology and fluid content. The G term, and especially the negative sign in front of the second term, is of interest for fluid detection. The reason is that the $\frac{\triangle \mu}{\overline{\mu}}$ term is approximately twice as large as the $\frac{\triangle V_{P0}}{\overline{V}_{P0}}$ term in a lithological transition. The result is that G has an opposite sign compared to R_0 (Thomsen, 2002). However, in a fluid transition $\frac{\triangle \mu}{\overline{\mu}} \approx 0$ and the sign of the two coefficients correspond.

3.4.3 AVO classification

Rutherford and Williams (1989) created a classification scheme for the AVO response for various gas sands. Avseth et al. (2010) suggest using the same classification scheme as a representative system without necessarily linking them to gas sands. This to use the scheme for lithology and pore fluid separation. The AVO response can be characterized by crossplotting the reflectivity against the angle of incidence, as illustrated in Figure 3.4a. However, it might be easier to distinguish the classes on an intercept versus gradient crossplot given in Figure 3.4b.

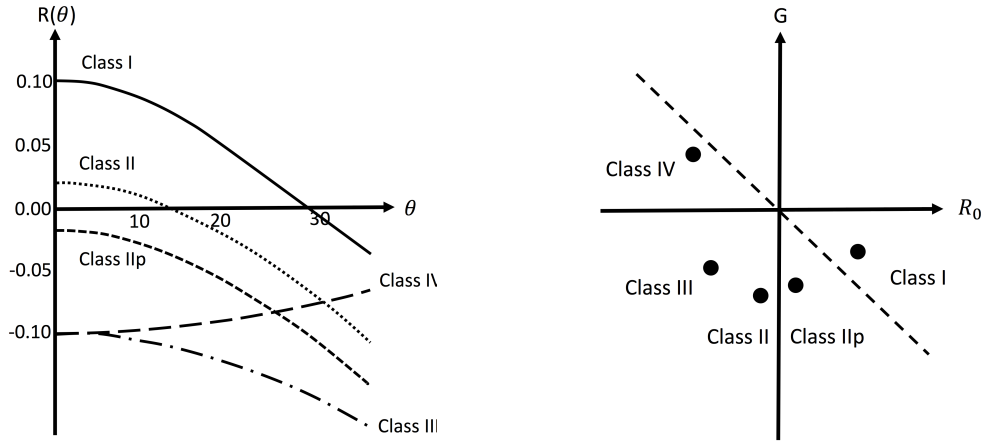

(a) $R(\theta)$ versus θ crossplot.

(b) R_0 versus G crossplot

Figure 3.4: The figures demonstrate the original AVO classes (I, II and III) defined by Rutherford and Williams (1989), along with the added classes, class IV (Castagna and Smith, 1994) and IIp (Ross and Kinman, 1995). Figure 3.4a is modified from Castagna and Swan (1997) and Figure 3.4b from Avseth et al. (2010).

The different AVO types are summarized in Table 3.2.

The classification system describes an underlying sand unit capped by a shale. This as the classification scheme was created to understand the link between a gas sand and the corresponding cap rock. Class I plots in the 4th quadrant with a positive intercept and a negative gradient. The class describes a high impedance sand compared to the overlying shale unit. Class IIp can be found in the same quadrant but with a smaller intercept value. The result is a polarity change with offset, and the class will disappear on a full stack section (Avseth et al., 2010). The 3rd quadrant shows class II and class III. Class II has a small negative intercept and a negative gradient giving a low impedance contrast between the sand and the overburden shale. Class III has a relatively high negative intercept and gradient. The sand has a lower impedance than the overlying shale and is often associated with bright spots (Avseth et al., 2010). The final class can be observed in the 2nd quadrant, class IV. The class has a negative intercept but positive gradient. The class is relatively rare but may occur when a hard shale caps a soft sand. Note that class III and IV may have identical normal incidence reflection coefficients (Fig.3.4a).

A brine filled rock might show increasing or decreasing AVO response. Interpretation of several intercepts and gradients will, for a brine-filled reservoir, follow a well-defined background trend (Castagna and Swan, 1997). Deviations from this pattern are defined as AVO

Table 3.2: AVO behavior for different AVO classes.

Class	Relative Impedance	Quadrant	R_0	G	AVO product
I	High impedance	4	+	-	Negative
II	No or low contrast	3	-	-	Positive
IIp	No or low contrast	4	+	-	Negative
III	Low impedance	3	-	-	Positive
IV	Low impedance	2	-	+	Negative

anomalies and can be related to hydrocarbons or other lithological factors. The latter one is associated with changed porosity or rock properties of the sand and shale. The distance from the fluid line depends on the contrast of the ratio of the P- and S-wave velocity (V_p/V_s) (Foster et al., 2010). The ratio is a function of pore compressibility and replacing brine with a more compressible fluid increases the S-wave velocity. Consequently, this reduces the V_p/V_s of the rock and displaces the AVO response away from the fluid line. The effect of changes in rock properties is illustrated in Figure 3.5.

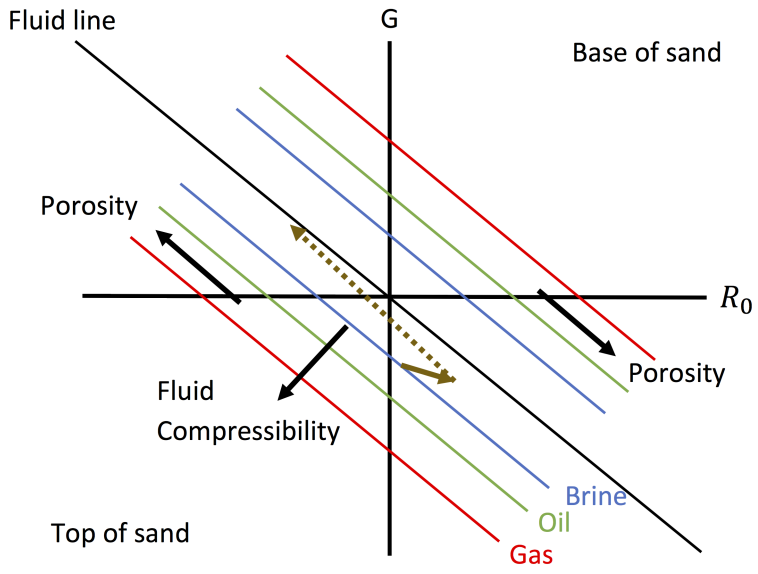

Figure 3.5: Effect of changes in reservoir properties on the AVO response. An increase in fluid compressibility displaces the response further away from the fluid line. An increase in porosity moves the response parallel to the trend, as displayed by the arrows. The solid brown line shows the effect of increased shale content in the sand layer, while the dashed brown line indicates the effect of adding clay to the pore content. The Figure is modified from (Foster et al., 2010).

3.4.4 Seismic AVO response - an expression of noise

Real seismic data contains a certain amount of noise, measured by the signal to noise ratio (S/N). Hendrickson (1999) demonstrate that the gradient term, calculated from the AVO response, is significantly more sensitive to noise than the intercept term. Further, the noise for the high angle coefficients only increases. It is hard to estimate the S/N ratio within the angle gathers since there are many possible contributors, among others coherent noise, multiples and overburden/transmission effects.

If data from several gathers with the same reflection extracted are plotted, will the expected crossplot response have an oval distribution of points around the real location, referred to as the noise ellipse (Simm et al., 2000). The reason is the sensitivity of the gradient term to noise. According to Simm et al. (2000) should the noise trend be easily recognized on real data, particularly by crossplotting samples from the same horizon from a seismic section.

Chapter 4

Methodology

4.1 Well Log Data and Upscaling

The well logs available for study at a depth of the Utsira formation was introduced in Section 2.2. Well 15/9-13 is used to analyze the AVO response, generate a synthetic trace and estimate rock properties for the reservoir model. To deliver the necessary parameters, additional well logs must be generated. This as the seismic response at an interface is primarily controlled by the seismic velocities, not directly measured by well 15/9-13. Although, the P-wave velocity log is derived from the sonic log by equation 4.1.

$$V_p = \frac{3,048 * 10^4}{\triangle t * 10^{-6}}, \tag{4.1}$$

where V_p is the P-wave velocity measured in km/s. A problem is the constant sonic log readings between 900-1050 meters. This as the other logs in the well identify several shale sequences in the same interval, which should affect the sonic log also. The consequence is that the P-wave velocity is manually corrected to be equal 2.2 km/s in the shale sequences. This is the velocity measured in the first major shale sequence within the Utsira formation. The sequences are interpreted using the caliper, density, and gamma ray log, in addition to NPDs lithology log by Normann and Østby (1982).

The S-wave velocity log is calculated by the Greenberg and Castagna equation. Two different equations are used dependent on lithology, equation 4.2 for sand layers and equation 4.3 for shale layers.

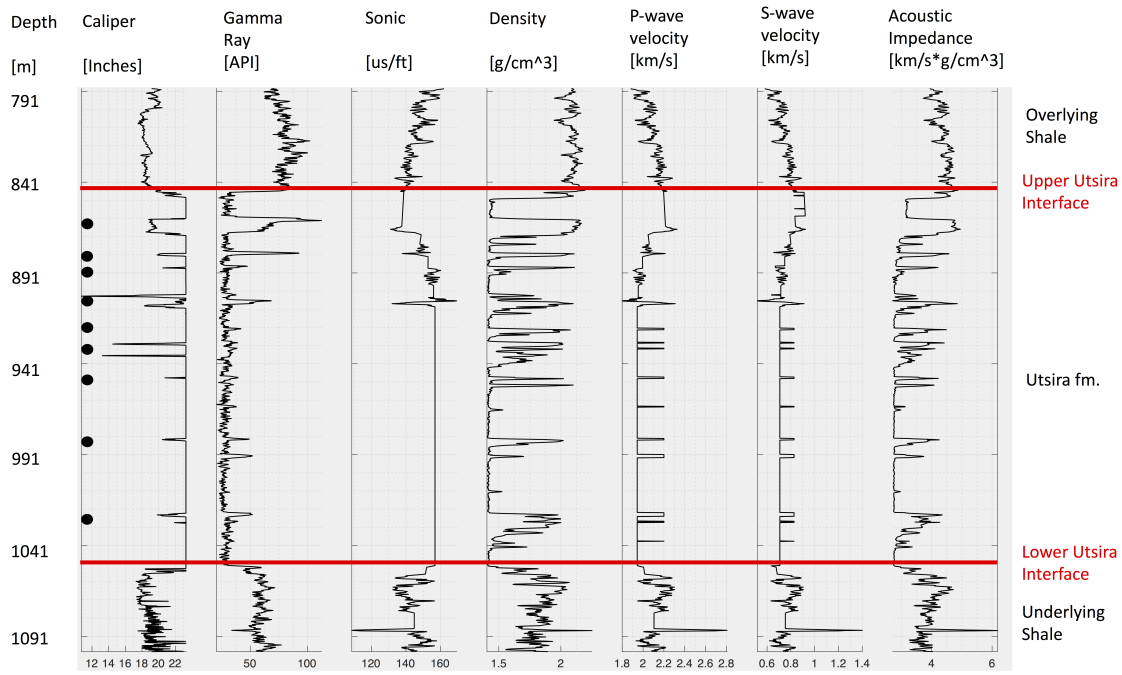

Figure 4.1: The original caliper, gamma ray, sonic and density log, in addition to the edited P-wave velocity, S-wave velocity, and acoustic impedance log. Note the markers to the right indicating the shale layers.

$$V_{s,sand} = 0.80416V_p - 0.85588, \tag{4.2}$$

$$V_{s,shale} = 0.76969V_p - 0.86735. \tag{4.3}$$

The prediction of the S-wave velocity is highly dependent on the quality of the estimated P-wave velocity.

Further, an acoustic impedance (I) log is generated by multiplying the P-wave velocity log with the density log. The log is used to generate a synthetic trace for correlation between well data and seismic data. The edited well logs are shown in Figure 4.1, together with the original well logs from well 15/9-13 at a depth of the Utsira formation.

Backus averaging method is performed to upscale the well log data. This to generate input parameters for the AVO analysis and the reservoir model. The requirements for the method is assumed to be fulfilled as the sample points from the well log data is defined as a VTI media. The generated anisotropy from the averaging method is a function of heterogeneity only. The sequences averaged are the overlying shale layer, underlying shale layer, and the Utsira formation. First, the elastic coefficients for each sample, j, are calculated using equation 3.10.

Table 4.1: Effective parameters from Backus averaging.

Formation	Interval $[m]$	$V_p[km/s]$	$V_s[km/s]$	$\rho[g/cm^3]$	ε	δ	γ
Over. Shale	790-847	2.0932	0.7391	2.0925	0.0032	-0.0045	0.0177
Utsira Fm.	847-1053	1.9689	0.7238	1.5563	0.0098	-0.0033	0.0286
Under. Shale	1053-1100	2.1079	0.7521	1.8187	0.0080	-0.0065	0.0341

Secondly, the effective elastic coefficients are calculated using equation 3.12. The effective velocities, density and anisotropic parameters are then calculated for the three formations in the sequence by using equation 3.14, 3.15, 3.16 and 3.17, respectively. The resulting effective parameters for the three intervals are summarized in Table 4.1.

4.2 Generating a Reservoir model

A reservoir model is generated to analyze the effect of fluid substitution in the Utsira formation. The substitution is performed between brine water and CO_2 in liquid form. Further, is it generated to get more reliable AVO results from a brine-filled Utsira formation. This as mistrust in the well log readings leads to uncertainties in the AVO response calculated from well log data. The reservoir model covers the overburden shale layer and the Utsira formation.

The properties of the overburden shale layer correspond to the effective properties derived from well log data. This as the data properties are of sufficient quality in the interval. The properties of the Utsira formation is partly taken from well log data and partly estimated. By this means that the internal shale layer properties are assumed to have the same properties as the overburden shale layer, while the sand layer properties are estimated by parameters representing the evident sand properties. The initial layer and fluid properties used in the model are presented in Table 4.2. The overburden shale layer and the internal shale layers are assumed to be anisotropic, while the sand layers in the Utsira formation are isotropic. Hence, the elastic coefficients are calculated using different equations, 3.10 for sand layers and 3.11 for shale layers. Estimation of the brine water properties is performed concerning temperature and pressure at a depth of investigation, and the assumed salinity.

The properties of the Utsira formation are calculated for different water saturations. The internal shale layers are assumed to have very low permeability, and fluid substitution in these layers are neglected. Hence, the velocities and density remain the same before and after substitution. This is not the case for the sand layers where brine water is deliberately replaced with

Table 4.2: Initial layer and fluid properties for the reservoir model.

Lithology / Fluid	K_{matrix} $[GPa]$	K_{frame} $[GPa]$	K_{fluid} $[GPa]$	μ $[GPa]$	ρ $[g/cm^3]$	V_p $[km/s]$	V_s $[km/s]$
Over. Shale	-	-	-	-	2.092	2.092	0.739
Utsira Sand	37	3.421	-	1.046	2.034	-	-
Utsira Shale	-	-	-	-	2.092	2.092	0.739
CO_2	-	-	0.104	-	0.780	-	-
Brine Water	-	-	2.514	-	1.021	-	-

carbon dioxide. The porosity of the sand layers is set to be 0.39. Further, the net to gross ratio in the Utsira formation is set to be $N/G = 0.9$. The ratio is estimated from well log data. Note that the fraction of shale is larger in the well log relative to the average ratio of the Utsira formation. The rock properties for different fluid saturations are calculated by the Gassmann equation.

Finally, the Backus averaging method is performed on the Utsira formation to get parameters for the AVO analysis. The method generates the effective velocities, densities and anisotropic parameters for different fluid saturations. Note that also the anisotropic parameters get affected by changes in fluid properties. This can be seen in equation 3.17. Also, note that the calculated effective anisotropies from the Utsira formation are a function of both initial anisotropies from the shale layers and the anisotropy generated from Backus averaging.

4.3 Correlation between Well Data and Seismic Data

The derived acoustic impedance (I) log is used to generate a synthetic trace. The trace works as a tie between the well data and the seismic reflection data. The relationship is valuable for determining the upper Utsira interface extracted from seismic data. First, the reflection coefficient (R_{pp}) from each sample point on the well log data is derived from the impedance log. The equation used is equation 4.4.

$$R_{pp} = \frac{I_2 - I_1}{I_2 + I_1}, \tag{4.4}$$

where I_1 and I_2 represent the acoustic impedance of the overlying and underlying unit of the interface, respectively. The resulting coefficients are shown in Figure 4.2a, together with the generated synthetic trace. The trace is created by convolving the reflection coefficients with a Ricker wavelet with a peak frequency of 30Hz. The frequency corresponds to the peak frequency of the seismic dataset.

Figure 4.2b shows the synthetic trace and the zero-offset traces from two gathers extracted from Angline1. The upper Utsira interface is represented by a trough or a negative amplitude. This is expected for the interface as the overlying shale unit is harder than the Utsira formation, comprised of unconsolidated sand. The upper Utsira interface is known on the reflection coefficient plot and accordingly on the synthetic trace. Further, correlation with seismic gathers tracks the interface on the seismic sections. The correlation also defines the polarity of the seismic data. Note that different polarity standards exist, explained in Herron (2011). The identified upper Utsira interface is quality controlled by comparing the common image point angle gather comparisons, shown in Appendix B with the analysis in Raknes et al. (2015a).

The interval covered by the synthetic trace do show good correlation with the true zero offset traces from Angline1. The upper Utsira reflector corresponds to the first major trough at approximately 850 meters on the synthetic trace. Further, the transition to the underlying shale sequence is interpreted to be the peak at about 1050 meters on the same trace. By comparing the synthetic trace to true traces, it becomes clear that the latter is slightly shifted in depth. The shift is approximately 25 meters up. The same observations are made for Angline2.

4.4 AVO analysis

4.4.1 AVO response from Well Log Data and Reservoir Model

The input parameters in the AVO equations are the effective medium properties calculated by Backus averaging. The AVO response from the well log data is estimated by using the isotropic and anisotropic weak contrast approximation described by Thomsen (2002) notation. This by using equation 3.23, 3.24, 3.25 and 3.22. Note that $\triangle\varepsilon$ and $\triangle\delta$ is zero in the isotropic approximation. Both the upper and lower Utsira interface are investigated from well log data. The response from the reservoir model is estimated by the Zoeppritz equation and the isotropic and anisotropic weak contrast approximation. The first by using equation 3.19, 3.20 and 3.18. The response is calculated for different water saturations with a $N/G = 0.9$. Further, the R_0, G and K terms are estimated by the least squares method for the Zoeppritz equation, with zero error. This to better compare the response with the isotopic weak contrast approximation.

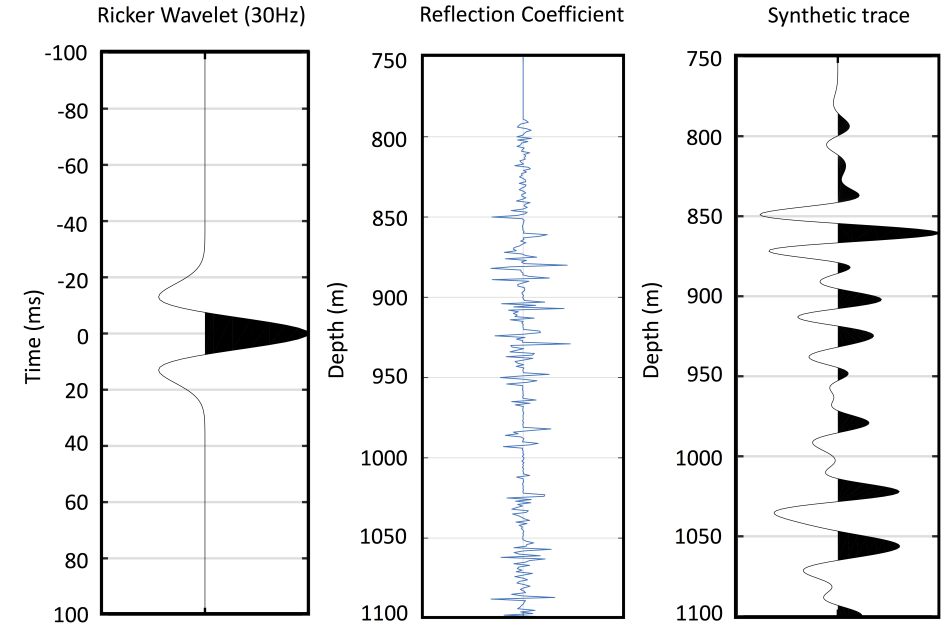

(a)

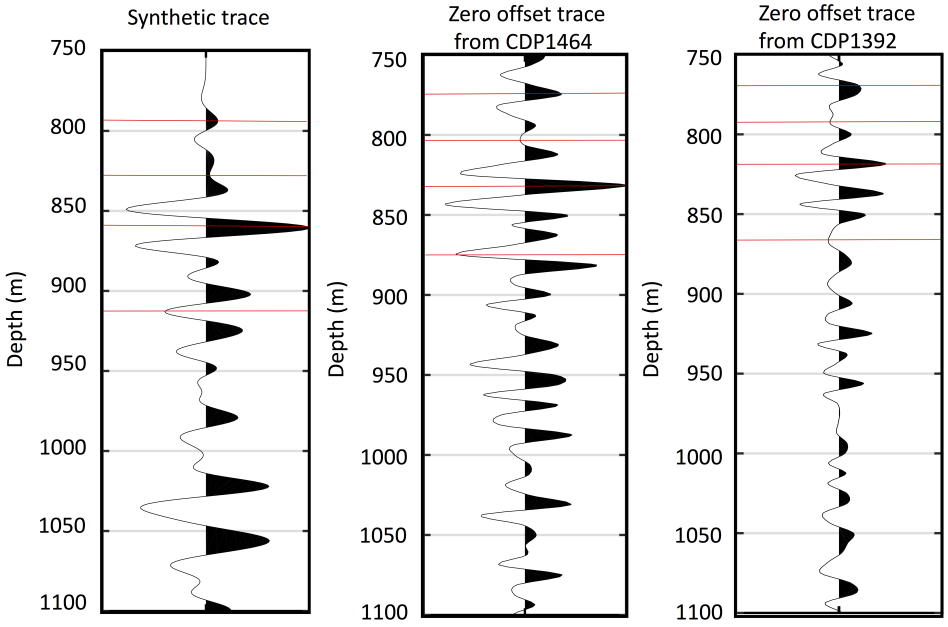

(b)

Figure 4.2: a) The Ricker wavelet to the left followed by the reflection coefficient and the generated synthetic trace. b) Comparison between the synthetic trace and two CDP gathers from Angline1.

4.4.2 AVO response from Seismic Sections

The AVO response from the seismic sections is gathered by extracting the upper Utsira interface from the seismic gathers. The responses are then smoothed to better observe and interpret the data. Besides, the smoothing reduces outliers and noise. The least squares method is performed on equation 3.22 to generate the smoothed response. The theory and calculations are presented in Appendix A. The benefit of the method is that the AVO response from the seismic data is shown by R_0, G and K terms. Implying that the response can be compared with the modeled response. Figure 4.3 shows the extracted and smoothed upper Utsira interface for two gathers from Angline1 and Angline2.

To better compare the modeled AVO response with the seismic response, the latter one is scaled. Firstly, the response from the CDP gathers with sufficient quality closest to well 15/9-13 is determined. This is CDP gather 1392 for both Angline1 and Angline2. Secondly, the CDP gathers are scaled with the modeled response from a fully brine saturated Utsira formation. This is done by equation 4.5.

$$A_s(\theta) = \frac{A(\theta) * R_{pp}(\theta = 0)}{A(\theta = 0)}, \tag{4.5}$$

where A_s is the scaled amplitude, A is the amplitude to be scaled, and R_{pp} is the modeled reflection coefficient. Then, the rest of the gathers from the seismic sections are scaled with respect to CDP gather 1392. The scaling requires that the Utsira formation in CDP gather 1392 is non-hydrocarbon bearing and representative for the area. With this mean that the gather is not taken from an area where a reservoir, strong structure, complex lithology or salt features are expected.

Figure 4.4a and 4.5a show the scaled intercept term, $R0$, calculated by the least squares method for each CDP gather on the two seismic sections. From the figures, one observes that some of the intercept calculations are significantly different than the average. There are several reasons for this discussed later. However, the goal is to investigate if these points are outliers or caused by other phenomena. Therefore, each AVO term for each CDP gather is smoothed. The smoothing method is an average smoothing including seven datapoints. The trend after smoothing is shown in Figure 4.4b and Figure 4.5b.

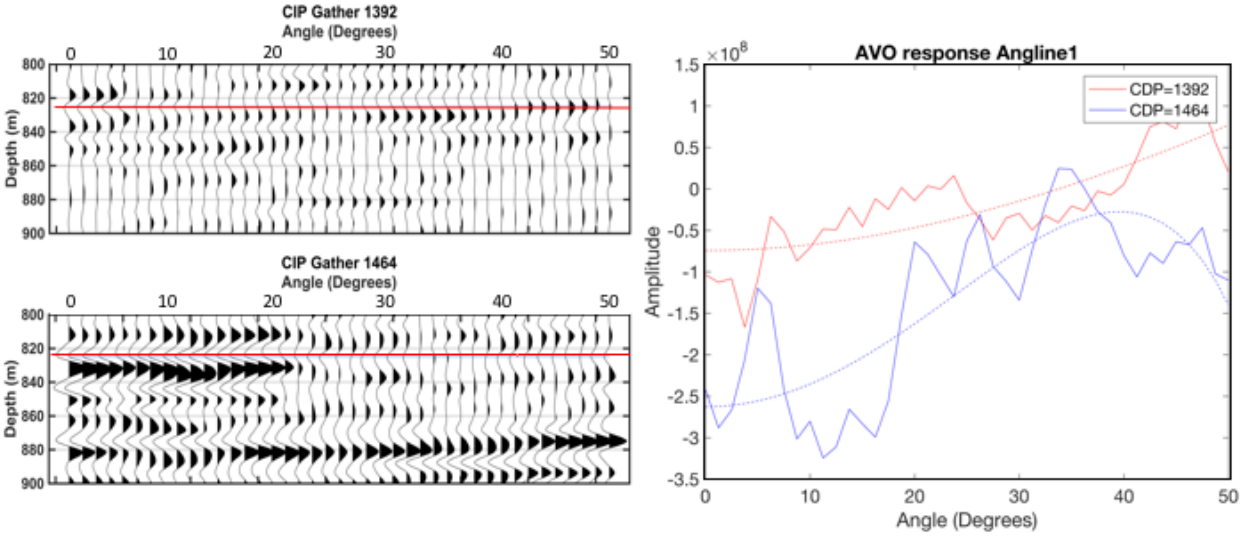

(a) Angline1

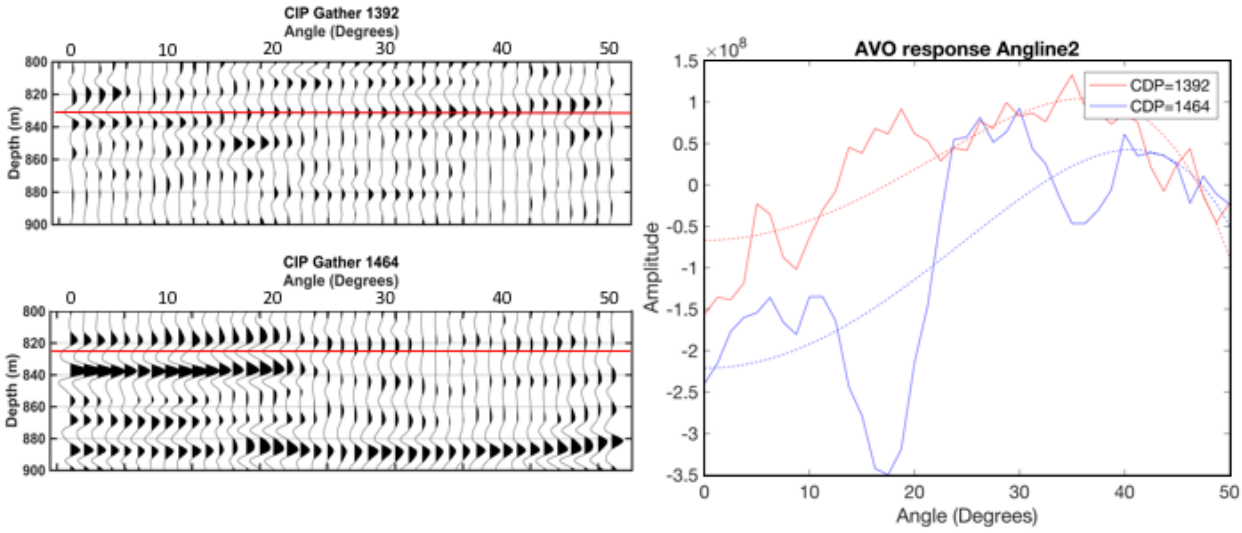

(b) Angline2

Figure 4.3: To the left: Extracted amplitudes from gather 1464 and 1393 for Angline1 and Angline2. To the right: Original and smoothed amplitudes from the upper Utsira reflection for the respective sections. Smoothing is performed by the least squares method.

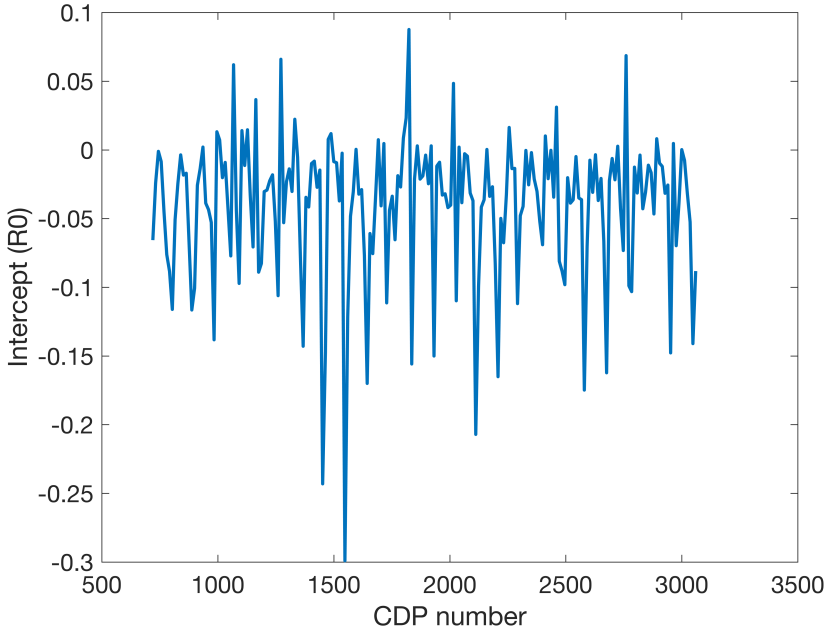

(a) Angline1

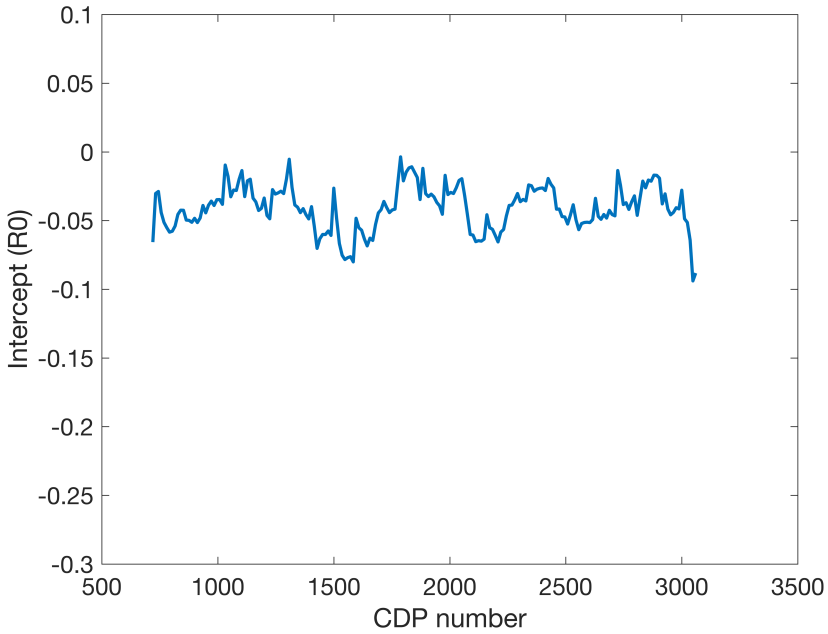

(b) Angline1

Figure 4.4: a) Calculated R_0 by the least squares method for each CDP gather. b) Smoothed R_0 by averaging the six closest datapoints.

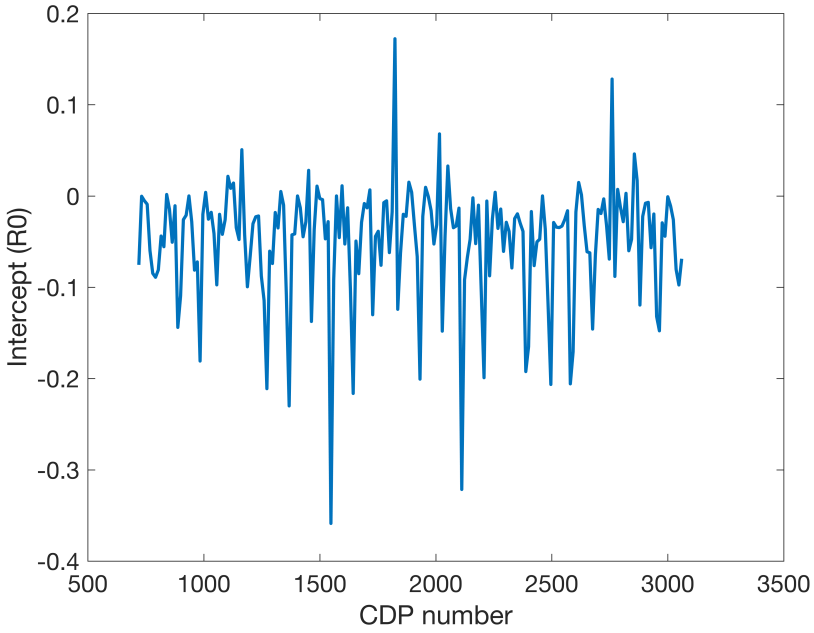

(a) Angline2

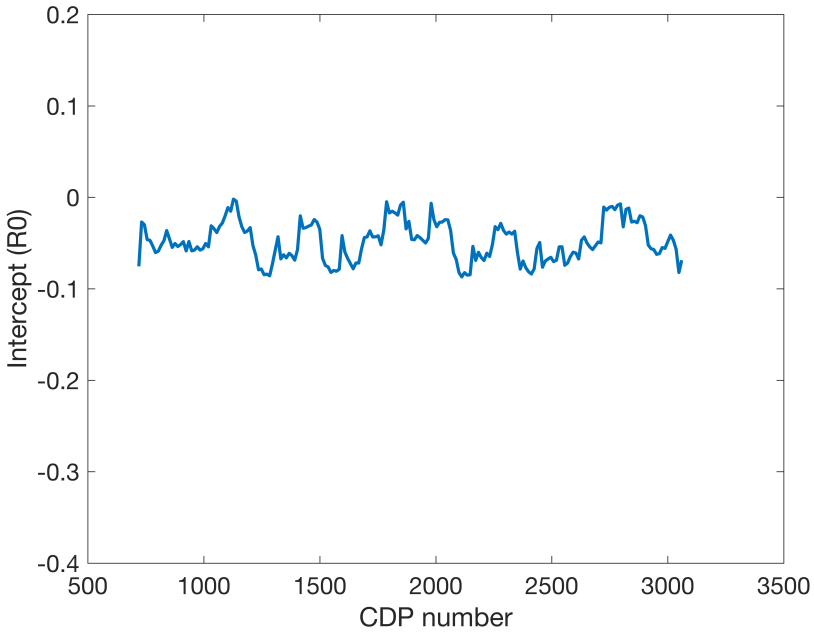

(b) Angline2

Figure 4.5: a) Calculated R_0 by the least squares method for each CDP gather. b) Smoothed R_0 by averaging the six closest datapoints.

Chapter 5

Results

5.1 The Effect of Fluid Substitution

The effect of fluid substitution in the Utsira formation of the reservoir model can be seen in Figure 5.1. Note that the fluid substitution is performed in the sand layers only and that the $N/G = 0.9$. The properties presented are for the effective reservoir medium, including the thin internal shale layers.

Figure 5.1a shows the P- and S-wave velocity as a function of fluid substitution. The P-wave velocity is most sensitive and decreases immediately as CO_2 substitutes water, but the reduction becomes less marked as the saturation increases. The drop is most intensive from $S_w = 1$ to $S_w = 0.8$, but continues to decline until $S_w = 0.1$. Then there is a marginal increase in P-wave velocity.

The rapid decrease in the P-wave velocity is caused by the direct relationship between the velocity and the bulk modulus. The bulk modulus of a brine saturated medium decreases rapidly with an increasing level of CO_2, observed in equation 3.3. Hence, the P-wave velocity decreases as well. However, the effect diminishes as the CO_2 level increases. As the effect decline, the relationship between the P-wave velocity and bulk density becomes dominant. Leading to an increase in P-wave velocity. The behavior is caused by a density decreases for increased CO_2 levels, shown in Figure 5.1b.

The opposite trend is observed for the S-wave velocity which increases with increasing CO_2 level. Equation 3.2 shows that the velocity is proportional to the shear modulus and inverse proportional to the bulk density. As the shear modulus is constant, the only factor controlling

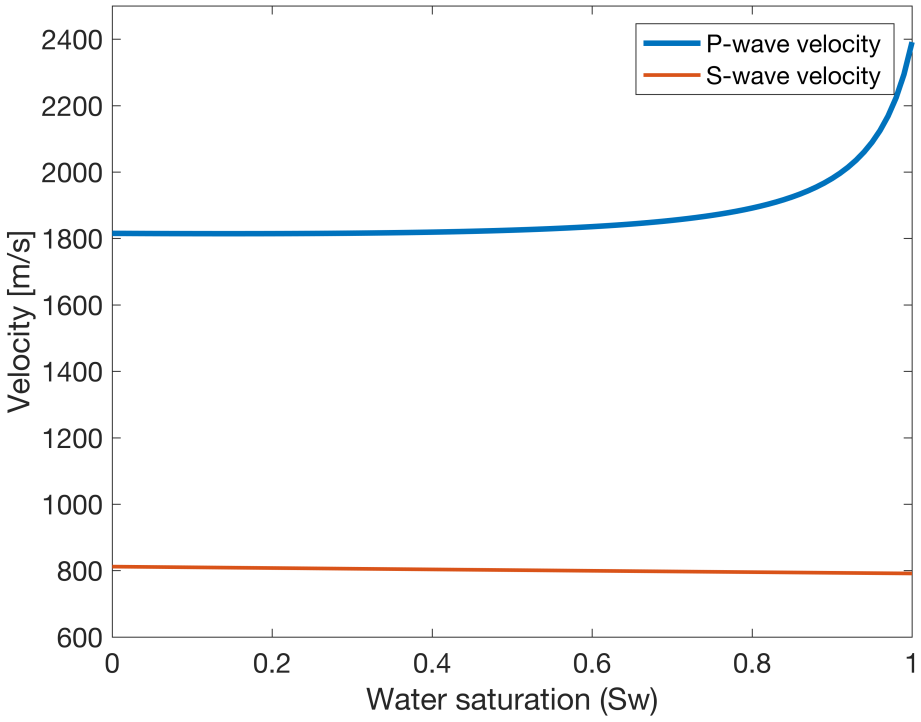

(a)

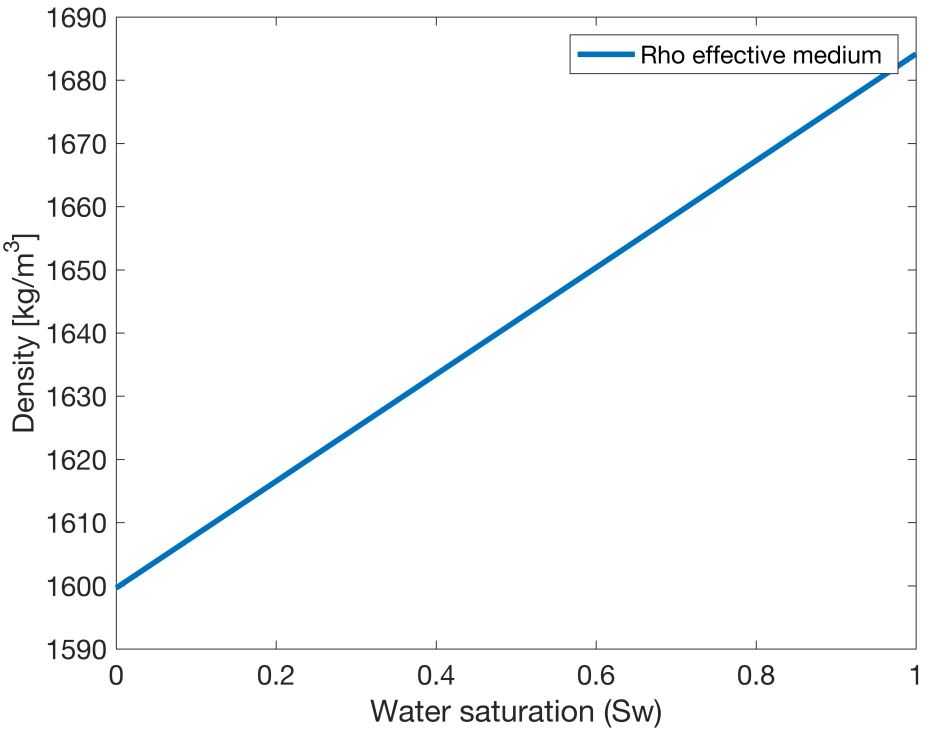

(b)

Figure 5.1: a) P- and S-wave velocities in the effective medium as a function of saturation. The fluid substitution is performed in the sand layers only. b) The density of the effective medium as a function of saturation. The fluid substitution is performed in the sand layers only.

the response is the bulk density. Hence, the S-wave velocity increases as the bulk density decreases for an increased amount of CO_2.

5.2 AVO response from Well Log Data

The modeled AVO response from the well log data represents a brine-filled Utsira formation. The result gives an indication of the response expected from the reservoir model and seismic gathers, despite the uncertainties in the well log readings. The AVO response from the Utsira formation is displayed in Figure 5.2. The response is calculated by the weak contrast approximation for both the isotropic and anisotropic case. The intercept for the upper Utsira formation is negative, as expected when going from a harder to a softer formation. Further, the amplitude variation with offset decreases for angles up to approximately 40 degrees before it starts to increase. Note that amplitude variation with offset refers to the change in magnitude of the reflection coefficient. Therefore, a negative reflection coefficient that becomes more positive will have a decreasing magnitude versus offset. The lower Utsira interface has the same behavior but with a positive intercept.

The AVO classification of the Utsira formation from the well log data is based on the upper Utsira interface. Figure 5.2 demonstrates that the AVO response going from the overlying shale into the Utsira formation gives a negative intercept, positive gradient and negative curvature. The relationship between the intercept and gradient classifies the Utsira formation as a typical class IV sand. This can be seen by comparing Figure 5.2 with Figure 3.4 from Section 3.4.

The most likely environment to observe a class IV anomaly is from unconsolidated sediments with a large V_p/V_s ratio. Hence, the analysis corresponds to the well log observations in Section 2.2. The upper Utsira interface has a relatively large reflection coefficient indicating a sizable drop in acoustic impedance.

Figure 5.2 also shows the response from the isotropic and anisotropic weak contrast approximation. One observes that including anisotropy in the AVO calculations does not lead to significant changes in the AVO response. Although, the effect becomes more pronounced for higher angles of incidence. This is expected as it is the G and K terms that include $\triangle\delta$ and $\triangle\varepsilon$, respectively. The jump in anisotropic parameters is defined in equation 5.1. Note that the velocities are calculated concerning anisotropy for both the isotropic and anisotropic approximations.

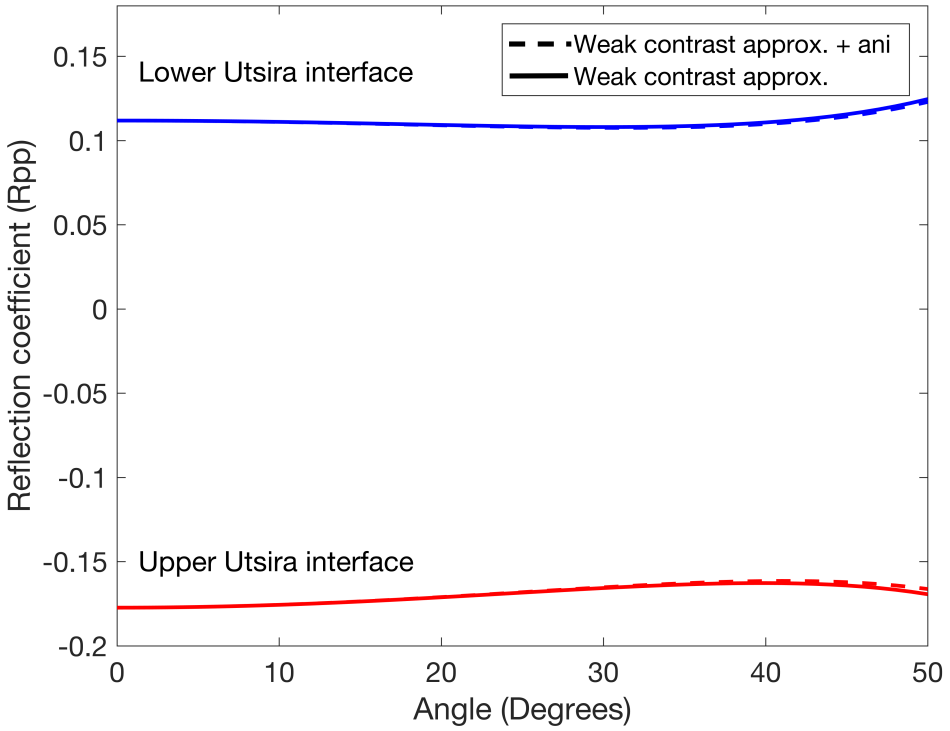

Figure 5.2: R_{pp}-θ plot describing the AVO response from the well log data. Both the upper and lower Utsira interface is plotted.

$$\begin{aligned} \triangle\delta &= \delta_2 - \delta_1, \\ \triangle\varepsilon &= \varepsilon_2 - \varepsilon_1, \end{aligned} \tag{5.1}$$

where δ_2 and ε_2 represent the anisotropies from the underlying media, δ_1 and ε_1 the anisotropies from the overlying media.

From Figure 5.2 one also observe that the effect of including anisotropy is to reduce the curvature for both interfaces. This as the upper and lower Utsira interfaces have a positive and negative jump in anisotropic parameters, with negative and positive reflection coefficients, respectively. The low impact of including anisotropy in the calculations is a result of a modest jump in anisotropic parameters. The initial effective anisotropies were displayed in Table 4.1.

5.3 AVO response from Reservoir Model

This section presents the AVO response calculated from the reservoir model. The response is from the upper Utsira interface between the Utsira formation, partially saturated by mixtures

of CO_2 and brine water, and the overburden shale layer. The Utsira formation is represented by the effective medium defined in Section 4.2. The response is calculated using the Zoeppritz equation and the weak contrast approximation for both an isotropic and anisotropic media.

Figure 5.3 shows the response for a full brine saturated medium compared to the response from the well data. The response from the reservoir model stands out when comparing the responses. This is primarily due to the edited properties in the reservoir model, changed to correct for uncertain well log readings. The change in properties affects the intercept, gradient and curvature as seen in Equation 3.23, 3.24 and 3.25, respectively. For example, will the intercept term become more positive as the first term in Equation 3.23 increases due to increased velocity in the Utsira formation. This corresponds to the observations in Figure 5.3.

Figure 5.3 also shows that the reflection coefficient for the isotropic and anisotropic weak contrast approximation almost overlaps completely. Hence, the effect of using the anisotropic weak contrast approximation is even less than for the well log data. Therefore, only the isotropic weak contrast approximation is further investigated. This is beneficial as it is directly comparable to the Zoeppritz equation, also an expression for the isotropic reflection coefficient.

There is an expected difference between the AVO response calculated by the Zoeppritz equation and the isotropic weak contrast approximation. This is because the latter is a weak layer contrast approximation. The approximation is quite close to the exact Zoeppritz equation at near angles but deviates for far angles. This is expected as the weak layer contrast is valid only for low angles of incidence. Therefore, the deviation increases as the angle increases.

Figure 5.4 shows the AVO response of the upper Utsira interface for fixed values of water saturations in the range of 0-1. The Figure shows the response calculated by the Zoeppritz equation only. The first thing to notice is the concave upward slope at $S_w = 1$. The magnitude versus angle decreases for angles lower than approximately 35 degrees before it starts to increase again. The AVO classification is equal the well log response and corresponds to a class IV sand. This changes as CO_2 is injected into the sand layers in the reservoir model. Then the intercept term abruptly becomes more negative with decreasing water saturation. Further, the slope goes from being concave upward to concave downward from $S_w = 1$ to $S_w = 0.9$, for all angles. The effect is a classification change from class IV sand to class III gas sand. Note the abrupt change in reflectivity from pre –to post-injection.

Figure 5.5 highlights the fact that the AVO method is less sensitive to changes in pore fluid as the water saturation decreases. Also, the difference between the two AVO equations is displayed

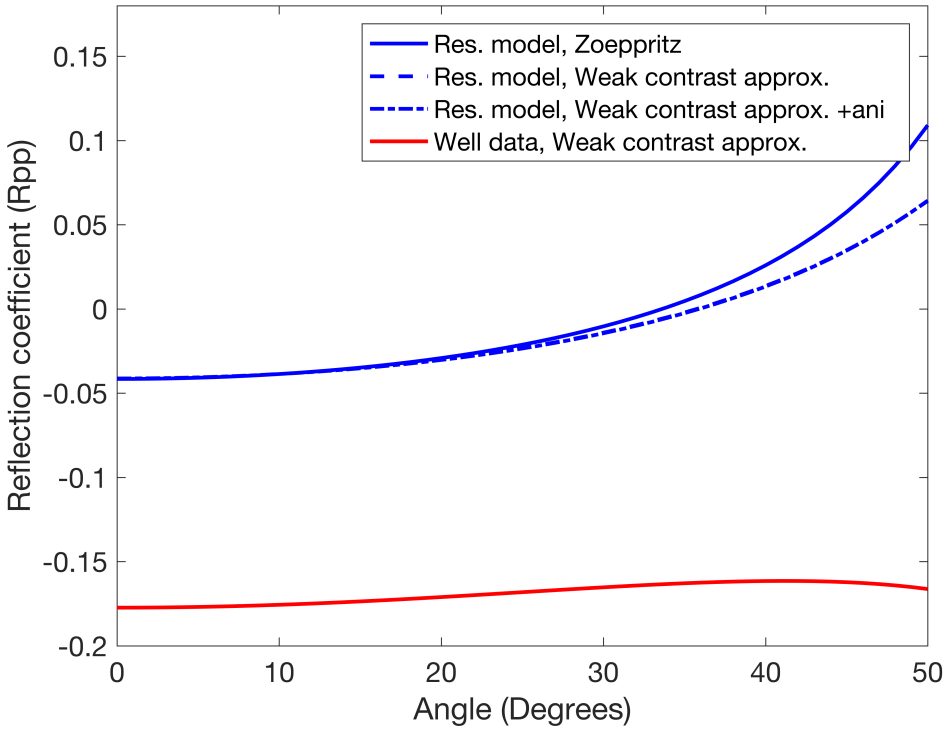

Figure 5.3: R_{pp}-θ plot describing the AVO response from the upper Utsira interface. The response is plotted for both the well log data and the reservoir model for a $S_w = 1$.

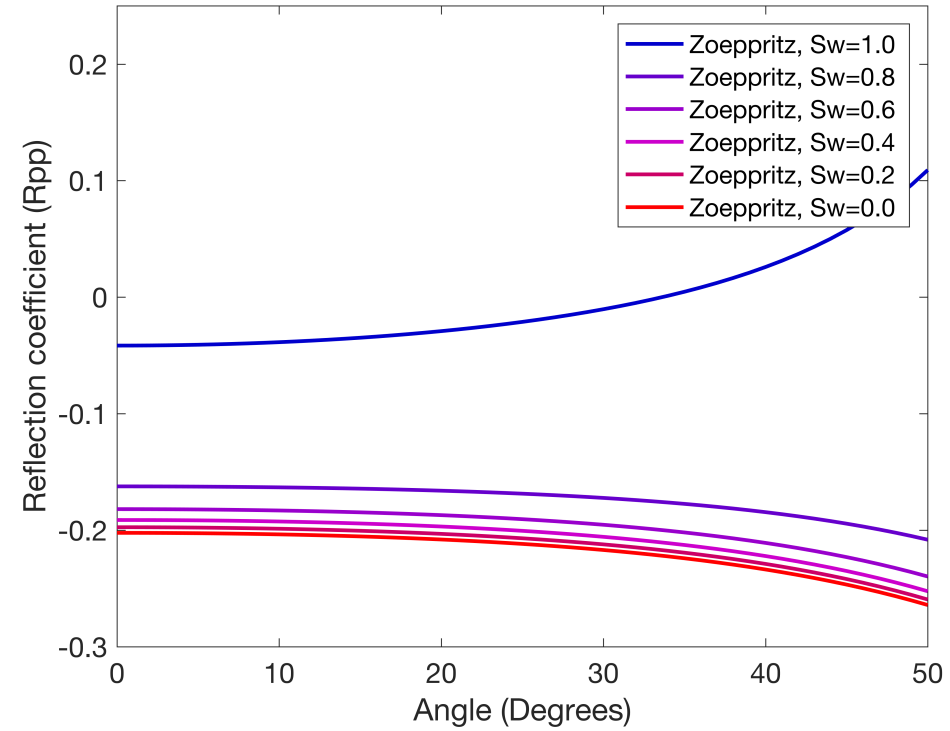

Figure 5.4: R_{pp}-θ plot describing the AVO response for different fixed partial CO_2 saturations.

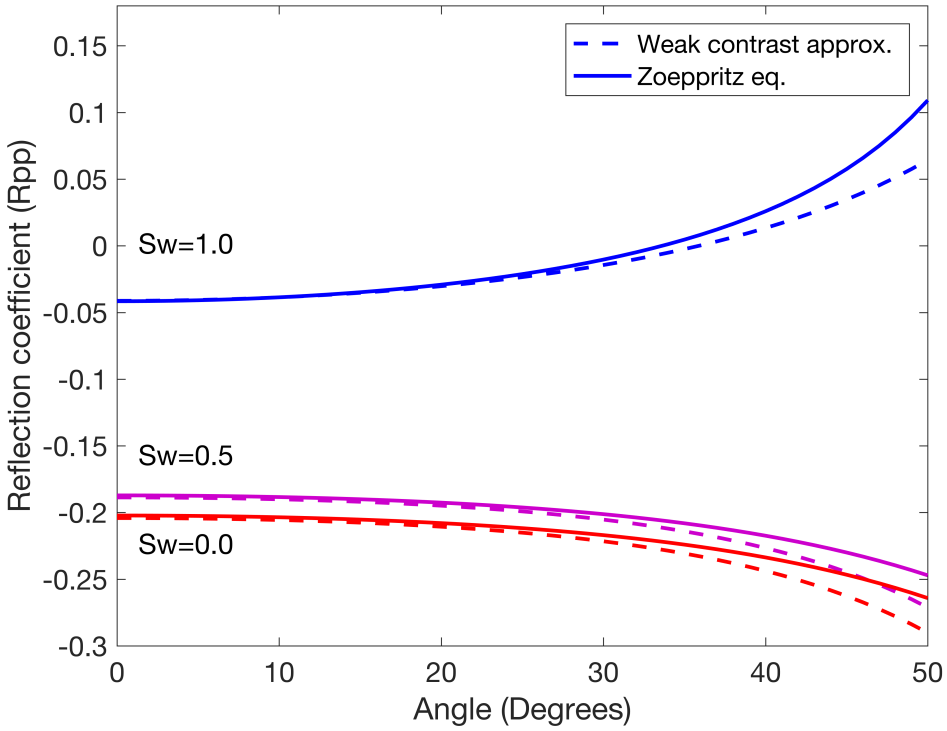

Figure 5.5: R_{pp}-θ plot highlighting the sensitivity for fluid substitution at high S_w values. Also, note the difference between the two equations used.

for different saturations. The Figure indicates that the difference between the two AVO methods decreases as the level of CO_2 increases. The magnitude of the intercept increases with 350.43% from $S_w = 1$ to $S_w = 0.5$ and only 8.07% from $S_w = 0.5$ to $S_w = 0$. The behavior is related to the changes in the velocities and density during fluid substitution, discussed in Section 5.1. Particularly the rapid P-wave velocity decrease at the beginning of the fluid substitution affect the AVO response. This because it leads to a rapid reduction in the impedance of the Utsira formation with respect to the overburden shale, moving the reflection coefficients toward more negative values. The effect ease as the velocity becomes less sensitive to fluid substitution at large CO_2 saturations. The response is further analyzed in Section 5.3.1.

5.3.1 AVO Crossplot Analysis

This section presents the results by crossplotting the intercept, gradient and curvature terms. Figure 5.6a shows the intercept versus gradient plot for the Zoeppritz equation, the isotropic weak contrast approximation, and the well data, respectively. The intercept is plotted on the x-axis while the gradient on the y-axis, the colorbar represents the water saturation. A full wa-

ter saturated medium is marked in blue while a full carbon dioxide saturated effective medium in red. The AVO response from the well data is marked as a black point with $S_w = 1$. The deviation from the modeled response is primarily due to a more negative intercept related to a higher contrast between the overlying shale and the Utsira formation. The contrast in the reservoir model is lower resulting in a less negative intercept. Note that the difference in gradient between the Zoeppritz equation and the isotropic approximation is larger for higher water saturations, as observed on the R_{pp}-θ plot.

Further, Figure 5.6a illustrates that both the intercept and gradient become more negative as CO_2 substitutes brine water in the effective medium. Replacing water with a more compressible fluid reduces the P-wave velocity of the rock. The compressible fluid leads to a decrease in density which increases the S-wave velocity. Thus, the CO_2 reduces the V_p/V_s ratio of the formation. This is the reason for the drastic changes in both intercept and gradient terms. It is important to stress that it is harder to discriminate between different fluids as the water saturation decreases, both on a R_{pp}-θ and R_0-G plot. However, it might be easier to classify the saturated reservoir formation on a crossplot.

Figure 5.6b shows the intercept versus curvature plot for the Zoeppritz equation, the isotropic weak contrast approximation, and well data, respectively. As predicted is the difference between the two AVO methods larger for the curvature term. This is because of the increased error for the weak contrast approximation for higher angles of incidence. As for the intercept and gradient terms, also the curvature becomes more negative as CO_2 substitutes brine water in the Utsira effective medium. From the crossplot, one observe that distinguishing between fluid saturations less than $S_w = 0.5$ is a difficult task. Though, the separation between a water filled medium and a CO_2 filled medium is significant. Note that the point representing the AVO response from the well log data is plotted close to the gas response from the reservoir model. The reason is the negative curvature term, observed in Figure 5.2. The sense of the behavior is associated with changed velocity and density properties in the Utsira formation, and not due to fluid substitution.

5.4 AVO Response from Angline1

The results from the AVO response of Angline1 is presented by R_0-G and R_0-K crossplots. Figure 5.7 shows the R_0-G crossplot while Figure 5.8 shows the R_0-K crossplot. Each point

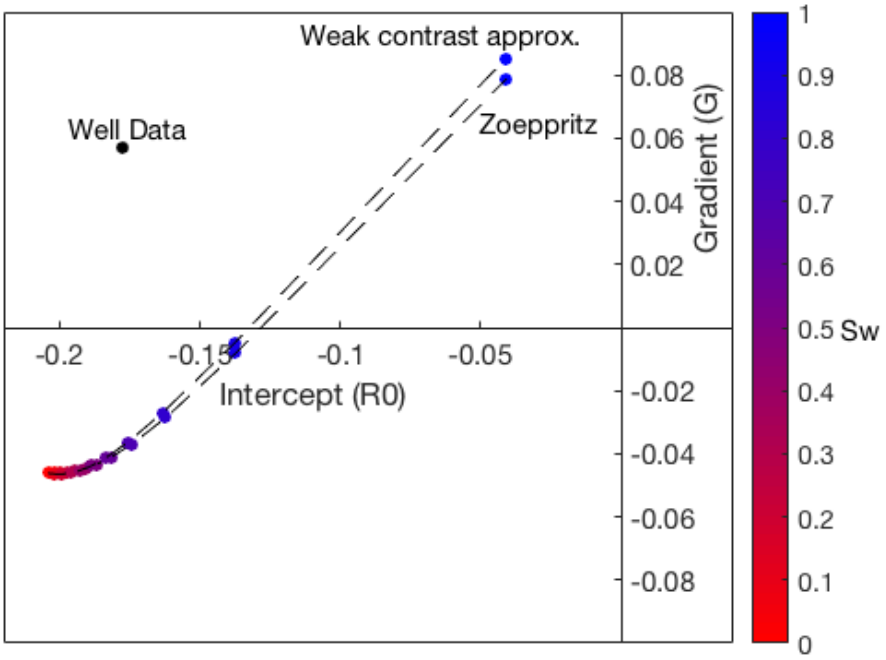

(a)

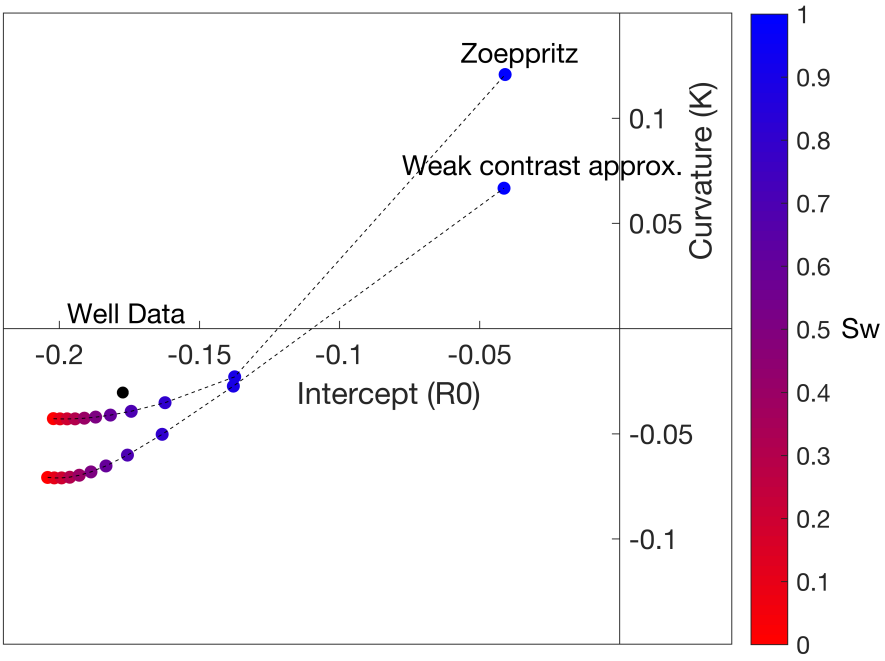

(b)

Figure 5.6: a) R_0-G crossplot for the well log data, Zoeppritz approximation, Zoeppritz equation, respectively. The two latter are modeled for different fluid saturations (Blue color represent S_w=1). b)R_0-K crossplot for the well log data, Zoeppritz approximation, Zoeppritz equation, respectively. The two latter are modeled for different fluid saturations (Blue color represent S_w=1)

on the plots represents the upper Utsira interface for a given CDP gather. Note that the result is the AVO response from a horizon and not a time window. The response is scaled with the response from the brine filled reservoir model. This as the dataset is gathered prior to injection and hydrocarbons or CO_2 are not expected to be present.

The general trend for the datapoints on the R_0-G crossplot is a negative intercept and a positive gradient. The area with the highest density is defined by $-0.1 < R_0 < 0.01$ and $-0.25 < G < 0.5$. The blue line crossing from the second to the fourth quadrant defines the background trend. The datapoints plotted close to this trend are assumed to represent a brine-filled Utsira formation. The response generates an oval distribution of datapoints around the background trend. This correlates with the estimated response due to noise, discussed in Section 3.4.4. The background trend is also approximated to be highly associated with the noise trend. Note that particularly the gradient term is sensitive to noise. Several datapoints stick out from the general trend. However, these are plotted alone and does not define a cluster of points. The latter would have been expected if another fluid were present in the section.

The curvature term varies between a negative and a positive response. The area with the highest density is defined by $-0.1 < R_0 < 0.01$ and $-0.25 < K < 0.25$. Note that the uncertainties in the measurements increase as the curvature term dominate the far offsets. This because of the terms sensitivity to noise, but also as the far offset amplitudes extracted from the seismic gathers are assumed to include larger error.

Figure 4.4b in Section 4.4.2 illustrated the smoothed intercept term with respect to the six closest datapoints for a given data sample. The reason for the smoothing is to remove outliers not representative for the interface and better observe the trends in the dataset. Figure 5.9 shows the R_0-G crossplot for the smoothed response. The first thing to notice is that the plot shows a higher density of datapoints close to the background trend. This is expected as the averaging method is performed. Further, all datapoints are in the same cluster confirming that the Utsira formation contains only brine water. The modeled response of the upper Utsira interface from the reservoir model by Zoeppritz equation is superimposed to the crossplot. This to demonstrate the expected response on real seismic data post injection of CO_2. The modeled response could also have been superimposed to the unsmoothed crossplot.

If the rock properties from Angline1 had been the same through the whole section, then the response would have been a single point plotted in the same area as the modeled brine saturated Utsira formation. However, this is not realistic due to changes in rock properties across the

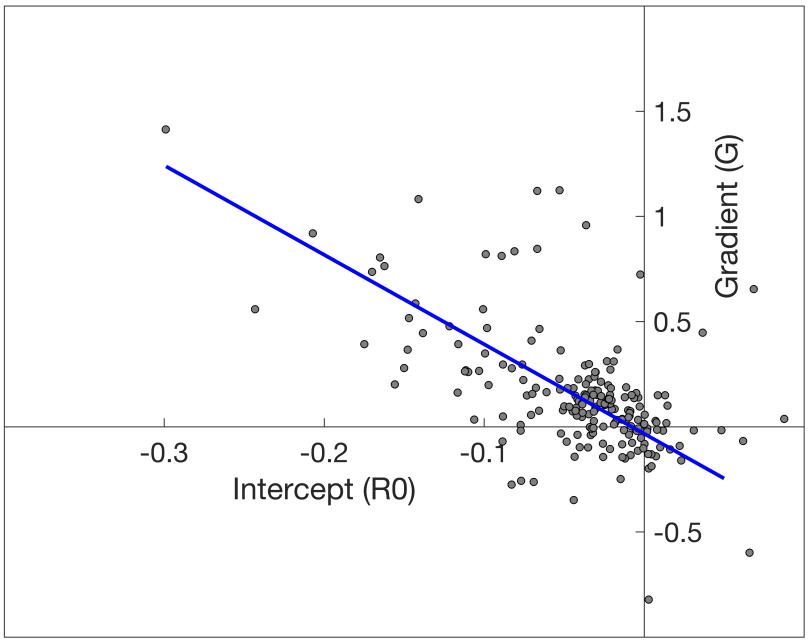

Figure 5.7: R_0-G crossplot for Angline1. The blue line represents the background trend.

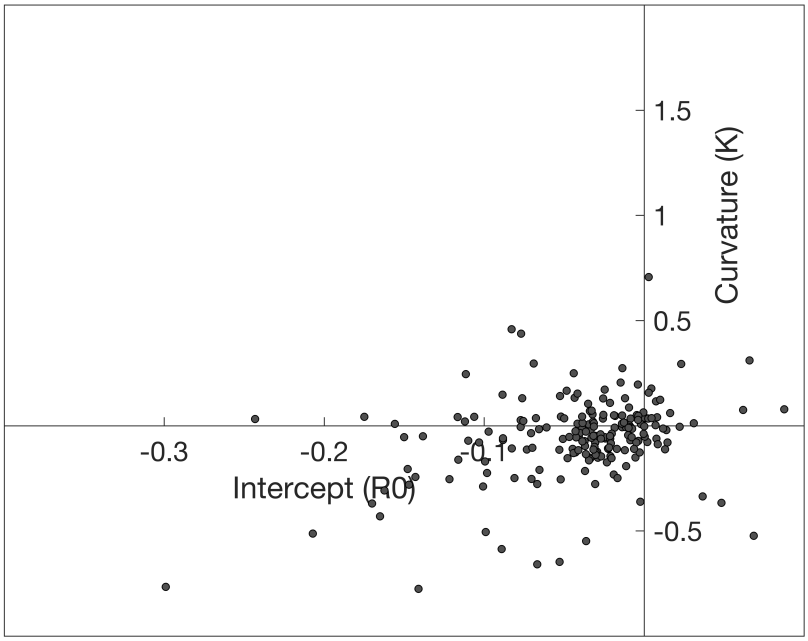

Figure 5.8: R_0-K crossplot for Angline1.

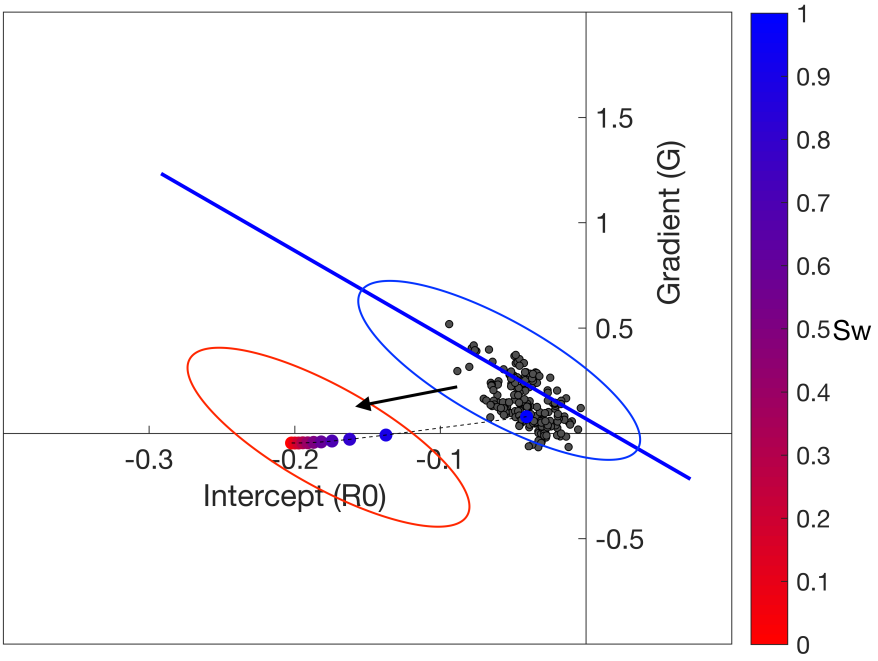

Figure 5.9: R_0-G crossplot for the smoothed datapoints from Angline1. The response from the reservoir model is superimposed on the plot.

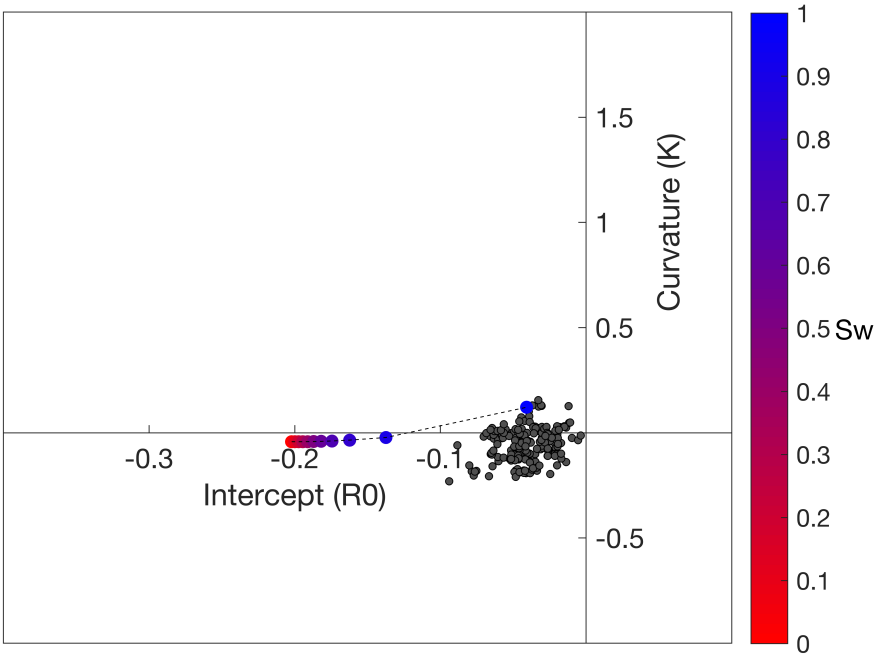

Figure 5.10: R_0-K crossplot for the smoothed datapoints from Angline1. The response from the reservoir model is superimposed on the plot.

section and noise. The effect of carbon dioxide injection would be to move the cluster of datapoints to more negative intercept and gradient values. Hence, a new data cluster would have been observed in the red circle from the gathers affected by the injection.

Figure 5.10 shows the smoothed R_0-K crossplot. Superimposed is the calculated fluid substitution response from the reservoir model. As for the R_0-G plot is the intercept terms from the data in the same range as the modeled brine saturated response. The range of the curvature terms, on the other hand, is not centered around the modeled response. This as most of the values is more negative from the real seismic gathers. The result confirms the uncertainties and increased error regarding the high offset reflection coefficients extracted from seismic gathers. The Figure shows that the effect of fluid substitution would have been a large change in intercept and minor change in the curvature to more negative values.

5.5 AVO Response from Angline2

Figure 5.11a shows the R_0-G crossplot from the upper Utsira interface extracted from Angline2. The same number of gathers are extracted from the section as for Angline1. The general trend for the datapoints is a negative intercept and a positive gradient. The area with the highest density of datapoints is defined by $-0.15 < R_0 < 0.0$ and $-0.3 < G < 0.5$. The datapoints plots around the background trend. No other trends are observed which confirms that the Utsira formation in the section is brine saturated. Hence, the same response as for Angline1.

Figure 5.11b shows the smoothed R_0-G crossplot from the upper Utsira interface. Superimposed to the plot is the modeled AVO response from the reservoir model for different fluid saturations. The data cluster corresponds to the modeled brine saturated Utsira formation. The effect of carbon dioxide injection would be, as for Angline1, to move the cluster of datapoints to more negative intercept and gradient values. The R_0-K crossplot is not displayed for this section as it does not bring more valuable information than the intercept and gradient terms.

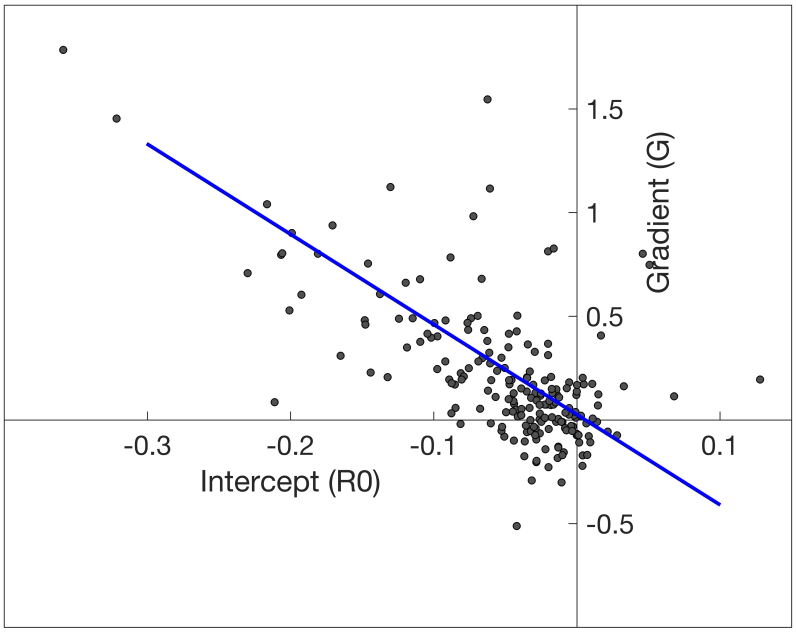

(a)

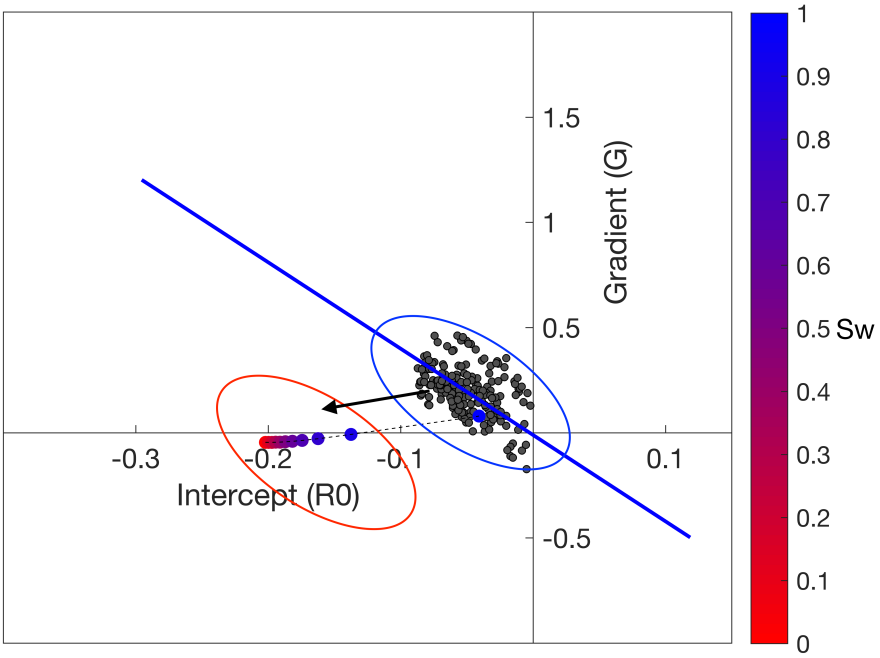

(b)

Figure 5.11: a)R_0-G crossplot for Angline2. b) R_0-G crossplot for the smoothed datapoints from Angline2. The response from the reservoir model is superimposed on the plot.

Chapter 6

Discussion

The AVO response from the upper Utsira interface analyzed for the well log data, reservoir model and seismic data are presented in chapter 5. The result is that all analyses classify the brine saturated Utsira formation as a class IV sand. Hence, an unconsolidated sand capped by a harder shale. This corresponds to the Utsira formation properties described in the literature. The result is encouraging for the reliability of the results. However, several uncertainties exist in all stages of the approach. Firstly, the low quality of the washed-out zones in the Utsira formation in the well logs. This indicates misreadings and underestimations of the rock properties. Also, comes the limitation of only four measurements in the well log data, mainly the lack of S-wave velocity information is unfortunate. Essentially as the Greenberg and Castagna equation assume pure monomineralic lithologies which are rarely the case.

The uncertainty from the well log data affects the reservoir model, comprising an overburden shale sequence and the Utsira formation. The latter generated by combining well log data and estimated parameters representative for the sand sequences. The velocity for the sand layers is computed based on the bulk modulus of the rock matrix. The resulting velocity for the brine saturated sand layers is 2.43 km/s, relatively high considering a density of only 1.63 g/cm^3. The effective velocity of the formation, including the thin shale layers, is 2.39 km/s with an effective density of 1.68 g/cm^3. Illustrating that the effective parameters are set to be significantly higher in the model than the well log readings. Despite the massive increase in velocity and density, is the reservoir model assumed to be representative for the geology close to well 15/9-13. However, the geology and physical properties are likely to vary moving laterally out from the well. This is not accounted for when comparing the AVO response from the model

with the response from the seismic sections.

The reason for generating the reservoir model is to investigate the AVO response during fluid substitution performed by the Gassmann equation. The equation includes some significant assumptions that are fulfilled in the reservoir model, but not in the real Utsira formation. For example, will not the Utsira formation have homogeneous mineralogy and be completely isotropic. The consequence is that the estimated rock properties post fluid substitution may not correspond to what the real rock properties post-substitution would have been. Despite this, is it still the preferred method in literature and the error is estimated to be minor compared to other limitations of the approach. During the substitution is the rate of carbon dioxide occupying the pore space increasing. For simplicity is it assumed that the carbon dioxide displaces the brine water in-situ leading to a two-phase saturation. Dissolution and chemical interactions between carbon dioxide and the rock matrix are not included. Ravazzoli and Gómez (2014) conclude that the assumption is fair due to the low amount of CO_2 expected to dissolve in brine water. Another issue is the state of the CO_2 after injection. This as CO_2 can appear in different phases in the subsurface varying within a given reservoir. For this thesis is a liquid phase estimated.

The modeled AVO response from the upper Utsira interface is analyzed for different fluid saturations by the Zoeppritz equation and the isotropic and anisotropic weak contrast approximation. The two latter ones to determine the effect of including anisotropy in the AVO equations. Note that the effective medium properties are calculated concerning anisotropy for both methods. The effect of including anisotropy in the weak contrast approximation turns out to be limited. Though, the relative difference increases as the reflection coefficients go toward zero. The limited differences are mainly because of the little variation in anisotropic parameters calculated for the over and underlying media. The result leads to usage of the isotropic weak contrast approximation only. The method is beneficial as it is directly comparable to the Zoeppritz equation. Comparison between the two methods is valuable to relax the core assumptions of the methods. The basic assumptions of the model upon which the Zoeppritz equation are based imply plane waves impinging on a planar, non-slip boundary between two isotropic and elastic semi-infinite half-spaces (Ursenbach, 2002). Because of the assumptions is not the Zoeppritz equation always accurate to describe real seismic responses. Although, the same can be said about the weak contrast approximation is it estimated to be equal or better for weak contrast interfaces.

The AVO response from the reservoir model is compared to the extracted amplitudes of

the upper Utsira interface from Angline1 and Angline2. The extraction of amplitudes from the seismic sections is also a source of error. This as the AVO method is sensitive to amplitudes caused by noise or acquisition and processing effects, including multiples and attenuation with depth. This means that outlying values in the amplitudes extracted create inaccurate estimates of the AVO parameters. The amount of noise is expected to be largest for high offset amplitudes, represented as the curvature term in the AVO analysis.

The AVO response is also highly affected if the CIP-gathers are curved. This might occur if the imaging is performed with an imprecise background velocity model. If this is the case, will not the chosen amplitude at high offsets be representative for the reflections extracted. Analyses of the seismic gathers indicate that most gathers are flat for the Utsira interface for both sections. The fact that both sections display the same AVO trends do also confirm this, as different velocity models are used for the sections. However, some of the gathers in both sections curve for high offsets. For example, CIP-gather 1392, shown in Figure 4.3b in Section 4.4.2. The result is large errors for the estimated curvature term in the AVO response.

Tuning caused by closely spaced boundaries is also a possibility. The tuning effect occurs for layers thinner than the tuning thickness, defined to be one-quarter of the dominant wavelength of the signal. The effect is that the upper and lower interface of a layer interfere and change the amplitude response. This might be a problem when extracting the upper Utsira interface from the seismic sections. This as the thickness of the sand layer between the overlying shale and the first internal shale layer is 14 meters at the well location. By assuming a lower estimate average velocity of 2.092 km/s and peak frequency of 30 Hz one get a tuning thickness of 17 meters. Note that an increased average velocity leads to greater tuning thickness. This indicates that the internal shale layer in the Utsira formation can result in interference of the upper Utsira interface. Further, will the relative distance between the reflections decrease with offset. In fact, the amplitudes may interfere for larger offsets even if they do not at small offsets (Avseth et al., 2010). The possible tuning effect is not corrected for in the AVO extraction.

Several other parameters can also affect the AVO response from seismic data. The limitations are well discussed in Avseth et al. (2010). Besides is a pre-processing scheme and pitfalls for AVO analysis presented.

Another aspect of the quality of the AVO response from the seismic gathers is the reliability of the reflections picked on the gathers. This as there is no confirmation that the reflections picked in the gathers are correct everywhere. This as the amplitude of the reflection varies from

gather to gather and can in some gathers be difficult to choose. The picking was performed automatically in MatLab, and a double check of every gather is almost impossible. If wrong reflections are picked for some gathers, this increases the error in the AVO crossplot analyses. However, there are reasons to believe that the percent of incorrectly chosen reflections are minimal. Mainly because of the flat geology and significant difference from overlying reflectors.

Avseth et al. (2010) express that the AVO method will work only if the rock physics and fluid characteristics of the target interface are expected to give a good response. For the AVO classification scheme is the classes defined for a sand capped by a shale. Assumptions reasonable for the interface investigated throughout the area. However, variability within the overlying shale might occur. Further, the unconsolidated sand layers of the Utsira formation with high porosity and permeability is expected to be unusually sensitive to injection of a more compressible fluid. Therefore, a presence of CO_2 induces a drop in velocity even for moderate saturations. This is beneficial when investigating the effect of fluid substitution by AVO analysis.

With all the potential uncertainties and limitations are the results still considered to be reliable and to quantitatively predict the changes that can be expected in the Utsira formation during fluid substitution. The approach is strengthened by the well log data analysis and the linking of the reliable reservoir properties to the reservoir model. The additional properties used for the sand layers of the Utsira formation are also acceptable for the area of investigation. Further, the AVO response from the seismic sections displays a good correlation with expected background trend and noise ellipse. The least squares method is expected to remove outliers and present the amplitudes extracted satisfactorily. The comparison between the modeled and real response supports the presumption that detectability of fluid substitution is likely to be observed. Also, the analysis of the real response confirms a full brine water saturated Utsira formation before injection.

Chapter 7

Conclusion

The aim of this thesis is to analyze the AVO response of the upper Utsira interface during fluid substitution. The thesis is intended to quantitatively predict the changes that can be expected for different saturations of carbon dioxide. Well log data, and a reservoir model is used as well as real seismic data prior to injection. The modeled AVO response from the reservoir model, for different saturations, are compared with the brine filled reservoir response from seismic data. The comparison demonstrates that the AVO method can be used for monitoring purposes as the method is sensitive to fluid substitution. As no data post injection are evaluated, similar analyses can be implemented for other geological sites before CCS projects.

The reservoir model consists of an overlying shale layer and the Utsira formation. The rock properties in the model are gathered from well 15/9-13, in addition to estimated parameters for specific sequences. The AVO response for the interface is calculated by the Zoeppritz equation and the isotropic and anisotropic weak contrast approximation. The latter ones to determine the effect of including anisotropy in the AVO equations. The result demonstrates that the effect is limited to the particular interface. The Zoeppritz equation and the isotropic approximation correspond at low angles but deviate for higher angles of incidence. This as the approximation is for weak contrasts and restricted to low angles of incidence. The deviation does not lead to changed AVO behavior.

The reservoir model is used to estimate the AVO intercept, gradient and curvature attribute with variable fluid saturation. The response is plotted on a R_{pp}-θ plot. The brine saturated Utsira formation has a negative intercept with a concave upward slope due to positive gradient and curvature terms. The AVO classification corresponds to a class IV sand. The response changes

significantly when CO_2 is injected into the reservoir. The intercept becomes more negative, and the slope becomes concave downward for all $S_w < 1$. The effect is a classification change from class IV sand to class III gas sand. The AVO response is most sensitive to fluid changes for low CO_2 saturations.

The trends are better observed on R_0-G crossplots. The intercept and gradient terms decay strongly for low CO_2 saturations. A loss of sensitivity for both parameters is observed for middle to high CO_2 saturations, mainly as the P-wave velocity stabilizes. The result suggests that accurate determination of CO_2 for $S_w < 0.5$ is challenging. The curvature and the R_0-K crossplot do not bring more valuable information than the intercept and gradient terms. Also, the error related to the parameter is significantly higher.

The AVO response of the upper Utsira interface extracted from Angline1 and Angline2 shows the trends expected. The noise ellipse expected on real datasets is well defined around the background trends for the brine saturated mediums on the R_0-G crossplots. By superimposing the modeled fluid substitution on the real datasets, it is observed that the AVO method can be used for monitoring. This as the effect of fluid substitution is to generate a cluster of datapoints at more negative intercept and gradient values, outside the noise ellipse. The result confirms that the AVO response from the upper Utsira formation is sensitive to fluid substitution. AVO analysis of real seismic data post injection of CO_2 is expected to give a good match with the modeled AVO response.

The extension of this work would include an AVO analysis of more seismic sections. Work to get access to data post injection would also be a priority. Finally, the extension would include the effect of frequency dependent AVO and tuning of thin layers.

Bibliography

Aki, K., Richards, P., 1980. Quantitative Seismology: Theory and Methods. No. v. 1 in A Series of books in geology. W. H. Freeman.

Avseth, P., Mukerji, T., Mavko, G., 2010. Quantitative seismic interpretation: Applying rock physics tools to reduce interpretation risk. Cambridge university press.

Backus, G. E., 1962. Long-wave elastic anisotropy produced by horizontal layering. Journal of Geophysical Research 67 (11), 4427–4440.

Banik, N., 1987. An effective anisotropy parameter in transversely isotropic media. Geophysics 52 (12), 1654–1664.

Berryman, J., 1997. Transversely isotropic elasticity poroelasticity arising from thin layers.

Berryman, J. G., 1999. Origin of gassmann?s equations. Geophysics 64 (5), 1627–1629.

Bjorlykke, K., 2015. Petroleum Geoscience: From Sedimentary Environments to Rock Physics. From Sedimentary Environments to Rock Physics. Springer Berlin Heidelberg: Berlin, Heidelberg, Berlin, Heidelberg.

Brown, S., Bussod, G., Hagin, P., 2007. Avo monitoring of co 2 sequestration: A benchtop-modeling study. The Leading Edge 26 (12), 1576–1583.

Castagna, J. P., Backus, M. M., 1993. Offset-dependent reflectivity—Theory and practice of AVO analysis. Society of Exploration Geophysicists.

Castagna, J. P., Smith, S. W., 1994. Comparison of avo indicators: A modeling study. Geophysics 59 (12), 1849–1855.

Castagna, J. P., Swan, H. W., 1997. Principles of avo crossplotting. The leading edge 16 (4), 337–344.

Chadwick, R., Noy, D., Arts, R., Eiken, O., 2009. Latest time-lapse seismic data from sleipner yield new insights into co2 plume development. Energy Procedia 1 (1), 2103–2110.

Chadwick, R., Zweigel, P., Gregersen, U., Kirby, G., Holloway, S., Johannessen, P., 2004. Geological reservoir characterization of a co 2 storage site: the utsira sand, sleipner, northern north sea. Energy 29 (9), 1371–1381.

Collet, O., Gurevich, B., 2013a. Fluid dependence of anisotropy parameters in weakly anisotropic porous media. Geophysics 78 (5), WC137–WC145.

Collet, O., Gurevich, B., 2013b. Fluid dependence of anisotropy parameters in weakly anisotropic porous media. Geophysics 78 (5), WC137–WC145.

Dupuy, B., Torres, V., Ghaderi, A., Milosz, E., Mezyk, M., 2016. Constrained avo for co2 storage monitoring at sleipner. 13th International Conference on Greenhouse Gas Control Technologies, GHGT-13, 14-18 November 2016, Lausanne, Switzerland.

Eiken, O., Brevik, I., Arts, R., Lindeberg, E., Fagervik, K., 2000. Seismic monitoring of co2 injected into a marine acquifer. In: SEG Technical Program Expanded Abstracts 2000. Society of Exploration Geophysicists, pp. 1623–1626.

Eskandari, H., Rezaee, M., Javaherian, A., Mohammadnia, M., 2003. Shear wave velocity estimation utilizing wireline logs for a carbonate reservoir, south-west iran. Iranian International Journal of Science 4, 209–221.

Foster, D. J., Keys, R. G., Lane, F. D., 2010. Interpretation of avo anomalies. Geophysics 75 (5), 75A3–75A13.

Furre, A.-K., Eiken, O., 2014. Dual sensor streamer technology used in sleipner co2 injection monitoring. Geophysical Prospecting 62 (5), 1075–1088.

Gassmann, F., 1951. Uber die elasticizat poroser medien. Vierteljahrsachr. Naturforsch. Ges., Zurich 96:1–23.

Greenberg, M. L., Castagna, J. P., 1992. Shear-wave velocity estimation in porous rocks: Theoretical formulation, preliminary verification and applications1. Geophysical Prospecting 40 (2), 195–209.

Hendrickson, J., 1999. Stacked. Geophysical Prospecting 47 (5), 663–705.

Herron, D. A., 2011. First steps in seismic interpretation. Society of Exploration Geophysicists.

Kumar, D., 2006. A tutorial on gassmann fluid substitution: formulation, algorithm and matlab code. matrix 2, 1.

Mahmoudian, F., Margrave, G. F., 2009. A review of angle domain common image gathers. Technical Report.

Miller, S. J., 2006. The method of least squares. Mathematics Department Brown University, 1–7.

Normann, T., Østby, J., 1982. WDSS 45 15 9 13: Completion report well 15/9-13 pl 046. Statoil/Esso/Norsk Hydro.

Ostrander, W., 1984. Plane-wave reflection coefficients for gas sands at nonnormal angles of incidence. Geophysics 49 (10), 1637–1648.

Pan, X., Gong, F., Cao, S., 2016. The interplay of avo and attenuation in seismic monitoring co2. In: SEG Technical Program Expanded Abstracts 2016. Society of Exploration Geophysicists, pp. 3052–3057.

Rabben, T. E., Ursin, B., 2011. Ava inversion of the top utsira sand reflection at the sleipner field. Geophysics 76 (3), C53–C63.

Raknes, E. B., Arntsen, B., Weibull, W., 2015a. Three-dimensional elastic full waveform inversion using seismic data from the sleipner area. Geophysical Journal International 202 (3), 1877–1894.

Raknes, E. B., Weibull, W., Arntsen, B., 2015b. Seismic imaging of the carbon dioxide gas cloud at sleipner using 3d elastic time-lapse full waveform inversion. International Journal of Greenhouse Gas Control 42, 26–45.

Ravazzoli, C. L., Gómez, J. L., 2011. Ava seismic reflectivity analysis in carbon dioxide accumulations: Sensitivity to co 2 phase and saturation. Journal of Applied Geophysics 73 (2), 93–100.

Ravazzoli, C. L., Gómez, J. L., 2014. Seismic reflectivity in carbon dioxide accumulations: A review. Carbon sequestration and valorization: InTech, 343–360.

Rider, M. H., 1996. The geological interpretation of well logs, 2nd Edition. Whittles, Caithness.

Ross, C. P., Kinman, D. L., 1995. Nonbright-spot avo: Two examples. Geophysics 60 (5), 1398–1408.

Rüger, A., 2002. Reflection coefficients and azimuthal AVO analysis in anisotropic media. Society of Exploration Geophysicists.

Rutherford, S. R., Williams, R. H., 1989. Amplitude-versus-offset variations in gas sands. Geophysics 54 (6), 680–688.

Simm, R., White, R., Uden, R., 2000. The anatomy of avo crossplots. The Leading Edge 19 (2), 150–155.

Stovas, A., Arntsen, B., 2003. Low frequency waves in finely layered media. In: 65th EAGE Conference & Exhibition.

Stovas, A., Landrø, M., Avseth, P., 2006. Avo attribute inversion for finely layered reservoirs. Geophysics 71 (3), C25–C36.

Thomsen, L., 1986. Weak elastic anisotropy. Geophysics 51 (10), 1954–1966.

Thomsen, L., 2002. Understanding seismic anisotropy in exploration and exploitation. Society of Exploration Geophysicists.

Ursenbach, C. P., 2002. Optimal zoeppritz approximations. In: SEG Technical Program Expanded Abstracts 2002. Society of Exploration Geophysicists, pp. 1897–1900.

Zoeppritz, K., 1919. On the reflection and propagation of seismic waves: Gottinger nachrichten, i, 66–84. Google Scholar.

Appendix A

Least Squares method

The least squares method is a mathematical regression analysis to find the line best fit for a given dataset. This is done by using simple calculus and linear algebra (Miller, 2006). The method is very useful in data fitting and assumes that the best fit curve to a dataset has the minimum sum of residuals squared, referred to as least square errors. Residual is defined to be the difference between the observed value and the value calculated by the method.

The least squares method is useful when comparing AVO responses from well log data, reservoir models and seismic data. The best fit line can be on a linear form or non-linear form depending on the data points and polynomial chosen to fit the data. For the AVO response, the best fit line is represented by the weak contrast approximation defined by Thomsen (2002). This too easily compare the results with the R_0, G and K terms. Hence, the weak contrast approximation is assumed to be the best fit for a dataset with $\{A_n, x_n\}$ where n is number of data points from $n = 1, N$. This is illustrated in equation A.1.

$$\begin{aligned} A(\theta) &= R_0 + Gsin^2(\theta) + K\frac{sin^4(\theta)}{1 - sin^2(\theta)}, \\ A(x) &= R_0 + Gx + K\frac{x^2}{1 - x}, \end{aligned} \tag{A.1}$$

where A represent the amplitude for a given angle and x is given by $x = sin^2\theta$. Note that R_0, G and K are unknown coefficients while all values of $A(x)$ and x are known. The best fitting curve, $\overline{A}$, to the dataset has the least squares error given by equation A.2

$$E = \sum_{n=1}^{N}(A_n - \overline{A})^2 = \sum_{n=1}^{N}(A_n - R_0 - Gx_n - K\frac{x_n^2}{1 - x_n})^2. \tag{A.2}$$

From the equation, it is clear that the squared deviation from each data point is summed to get the error. However, the goal is to find the coefficient values minimizing the error. This is done by differentiating the error, illustrated in equation A.3.

$$\begin{aligned}
\frac{\partial E}{\partial R_0} &= -2\sum_{n=1}^{N}(A_n - R_0 - Gx_n - K\frac{x_n^2}{1-x_m}) = 0, \\
\frac{\partial E}{\partial G} &= -2\sum_{n=1}^{N} x_n(A_n - R_0 - Gx_n - K\frac{x_n^2}{1-x_m}) = 0, \\
\frac{\partial E}{\partial K} &= -2\sum_{n=1}^{N} \frac{x_n^2}{1-x_n}(A_n - R_0 - Gx_n - K\frac{x_n^2}{1-x_m}) = 0.
\end{aligned} \tag{A.3}$$

Further, the equations can be rewritten (having divided by 2) and expanded as shown in equation A.4.

$$\begin{aligned}
0 &= \sum_{n=1}^{N} A_n - N_x R_0 - G\sum_{n=1}^{N} x_n - K\sum_{n=1}^{N}\frac{x_n^2}{1-x_n}, \\
0 &= \sum_{n=1}^{N} A_n x_n - R_0\sum_{n=1}^{N} x_n - G\sum_{n=1}^{N} x_n^2 - K\sum_{n=1}^{N}\frac{x_n^3}{1-x_n}, \\
0 &= \sum_{n=1}^{N} A_n\frac{x_n^2}{1-x_n} - R_0\sum_{n=1}^{N}\frac{x_n^2}{1-x_n} - G\sum_{n=1}^{N}\frac{x_n^3}{1-x_n} - K\sum_{n=1}^{N}\frac{x_n^4}{(1-x_n)^2}.
\end{aligned} \tag{A.4}$$

The unknown coefficients R_0, G and K can then be found by solving the set of equations. The resulting coefficients are given in equation A.5. By inserting the coefficients in equation 3.22 one get the best fit line for the AVO analysis of seismic data.

$$\begin{aligned}
R_0 &= \left[\frac{\sum_{n=1}^{N} A_n - G\sum_{n=1}^{N} x_n - K\sum_{n=1}^{N}\frac{x_n^2}{1-x_n}}{N}\right], \\
G &= \left[\frac{\sum_{n=1}^{N} A_n\sum_{n=1}^{N} x_n - K\sum_{n=1}^{N} x_n\sum_{n=1}^{N}\frac{x_{n^2}}{1-x_n} - N\sum_{n=1}^{N} A_n x_n + KN\sum_{n=1}^{N}\frac{x_n^3}{1-x_n}}{\left(\sum_{n=1}^{N} x_n\right)^2 - N\sum_{n=1}^{N} x_n^2}\right], \\
K &= \left[\frac{Q+P}{R+Z}\right],
\end{aligned} \tag{A.5}$$

where

$$
\begin{aligned}
Q = & \left(N \sum_{n=1}^{N} A_n x_n - \sum_{n=1}^{N} A_n \sum_{n=1}^{N} x_n \right) \times \\
& \left(\sum_{n=1}^{N} x_n^2 \sum_{n=1}^{N} \frac{x_n^2}{1-x_n} - \sum_{n=1}^{N} x_n \sum_{n=1}^{N} \frac{x_n^3}{1-x_n} \right), \\
P = & \left(\sum_{n=1}^{N} \frac{x_n^2}{1-x_n} \sum_{n=1}^{N} A_n x_n - \sum_{n=1}^{N} x_n \sum_{n=1}^{N} \frac{A_n x_n^2}{1-x_n} \right) \times \\
& \left(\left(\sum_{n=1}^{N} x_n \right)^2 - N \sum_{n=1}^{N} x_n^2 \right), \\
R = & \left(N \sum_{n=1}^{N} \frac{x_n^3}{1-x_n} - \sum_{n=1}^{N} x_n \sum_{n=1}^{N} \frac{x_n^2}{1-x_n} \right) \times \\
& \left(\sum_{n=1}^{N} x_n^2 \sum_{n=1}^{N} \frac{x_n^2}{1-x_n} - \sum_{n=1}^{N} x_n \sum_{n=1}^{N} \frac{x_n^3}{1-x_n} \right), \\
Z = & \left(\sum_{n=1}^{N} \frac{x_n^2}{1-x_n} \sum_{n=1}^{N} \frac{x_n^3}{1-x_n} - \sum_{n=1}^{N} x_n \sum_{n=1}^{N} \frac{x_n^4}{(1-x_n)^2} \right) \times \\
& \left(\left(\sum_{n=1}^{N} x_n \right)^2 - N \sum_{n=1}^{N} x_n^2 \right).
\end{aligned}
$$

Appendix B

Additional Figures

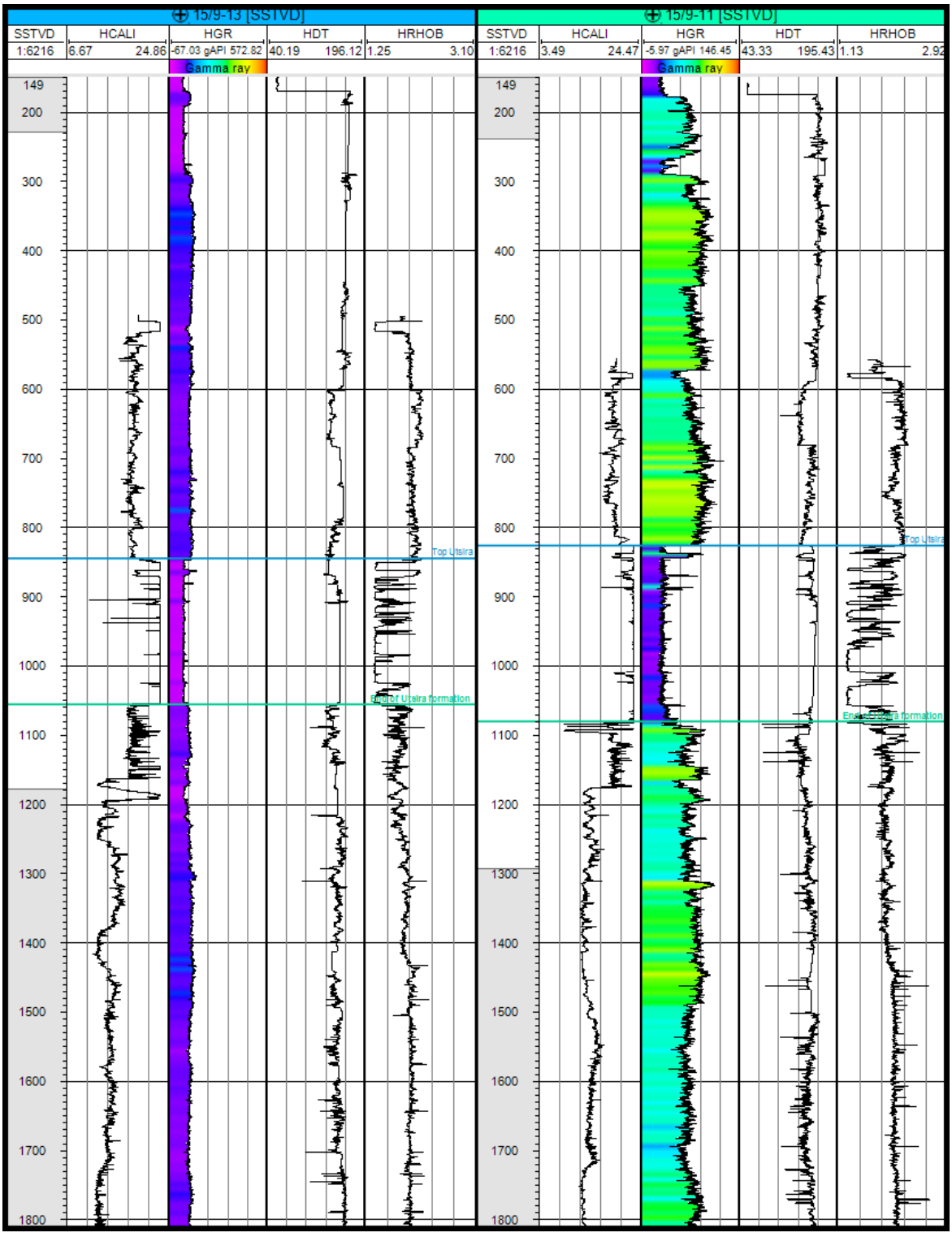

Figure B.1: To the left: Well log 15/9-13. To the right: Well log 15/9-11. The tracks are, from left to right, the caliper, gamma ray, sonic and density log. The logs are displayed from a depth of 149 to 1800 meters. The blue line represents the upper Utsira interface and the green line the lower Utsira interface. Note the change in particularly the gamma ray log for the Utsira formation.

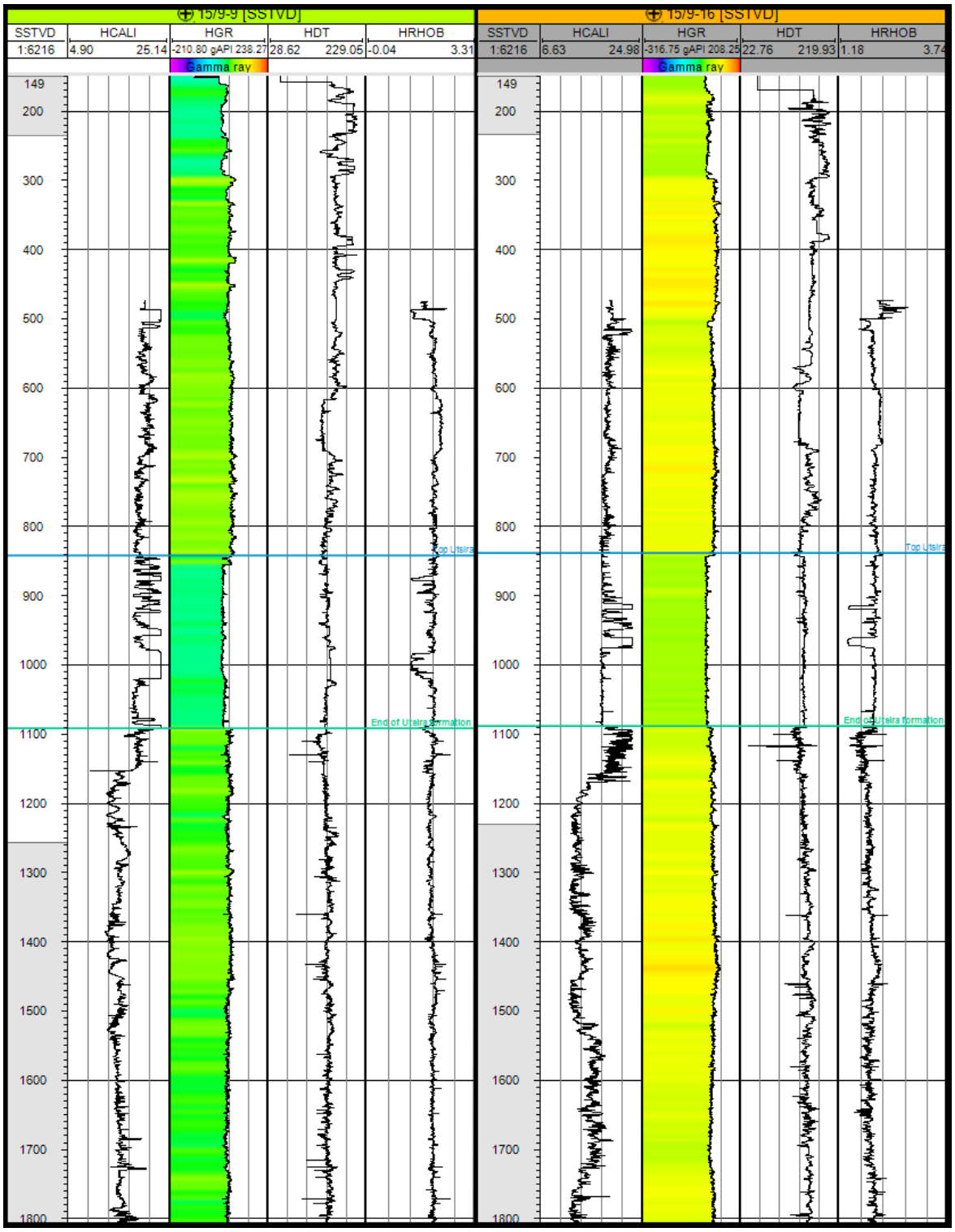

Figure B.2: To the left: Well log 15/9-9. To the right: Well log 15/9-16. The tracks are, from left to right, the caliper, gamma ray, sonic and density log. The logs are displayed from a depth of 149 to 1800 meters. The blue line represents the upper Utsira interface and the green line the lower Utsira interface. Note the change in particularly the gamma ray log for the Utsira formation.

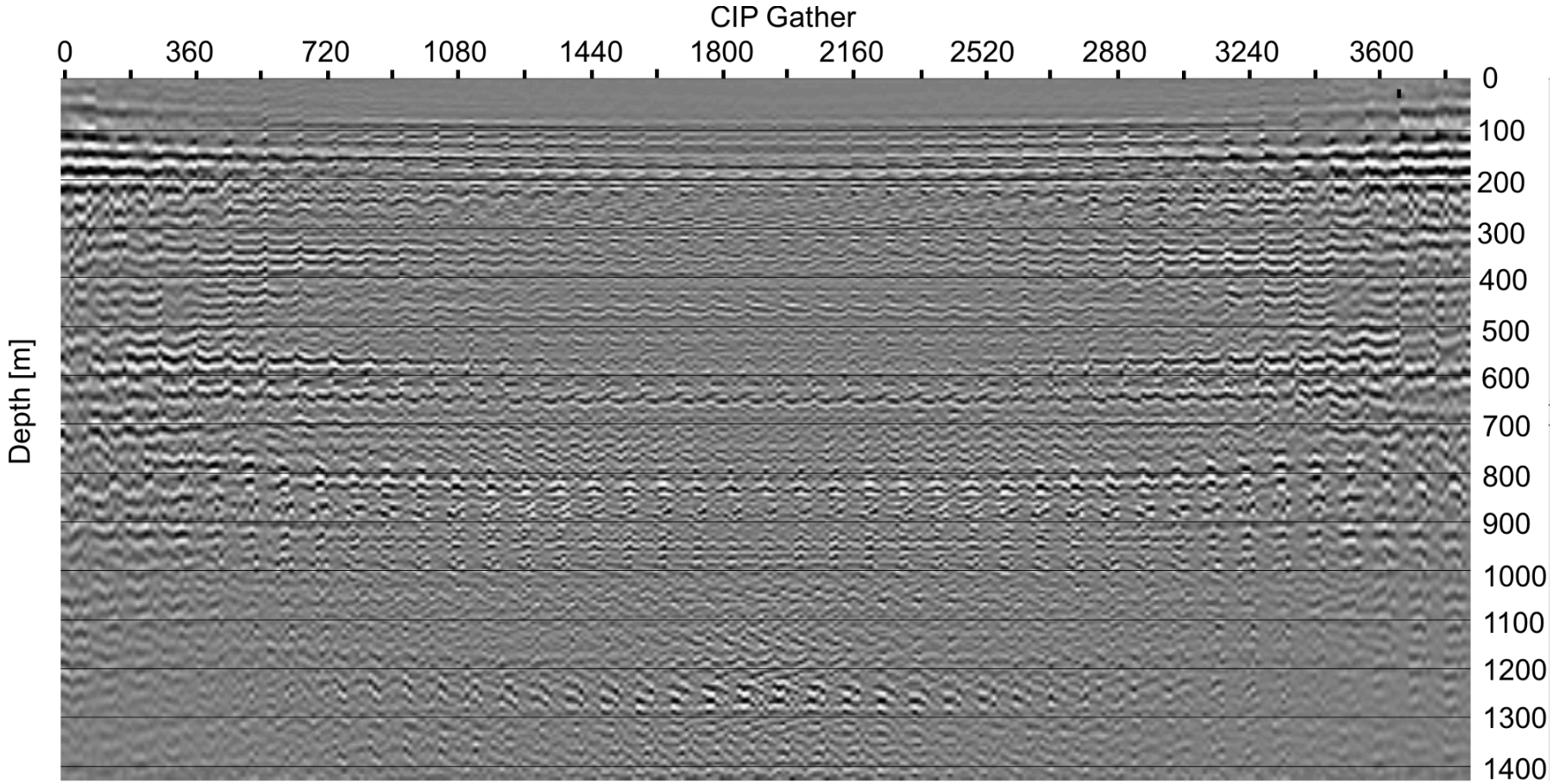

Figure B.3: Common image point angle gathers for Angline1. The angle axis is between -50 and 50 degrees.

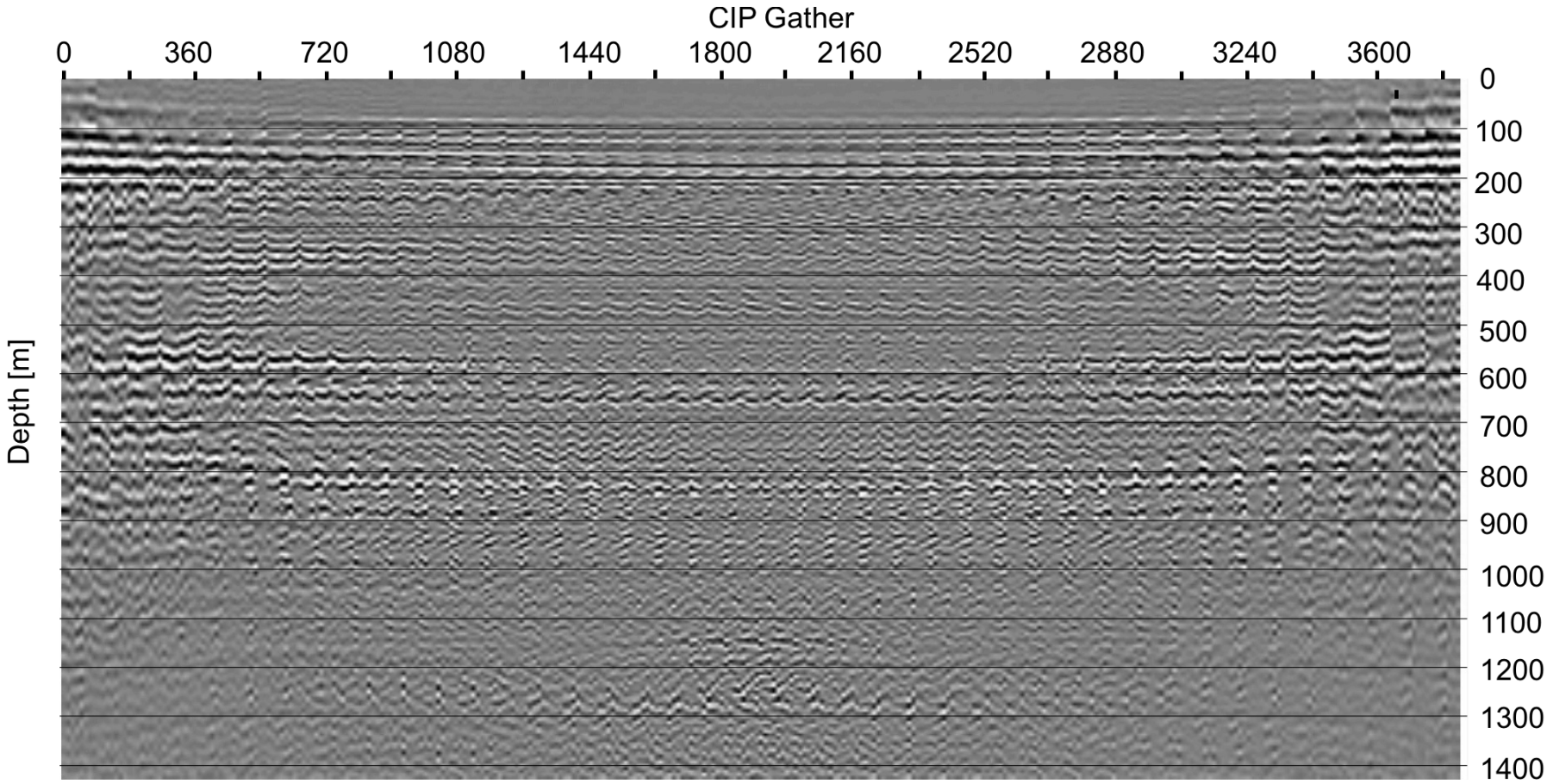

Figure B.4: Common image point angle gathers for Angline2. The angle axis is between -50 and 50 degrees.

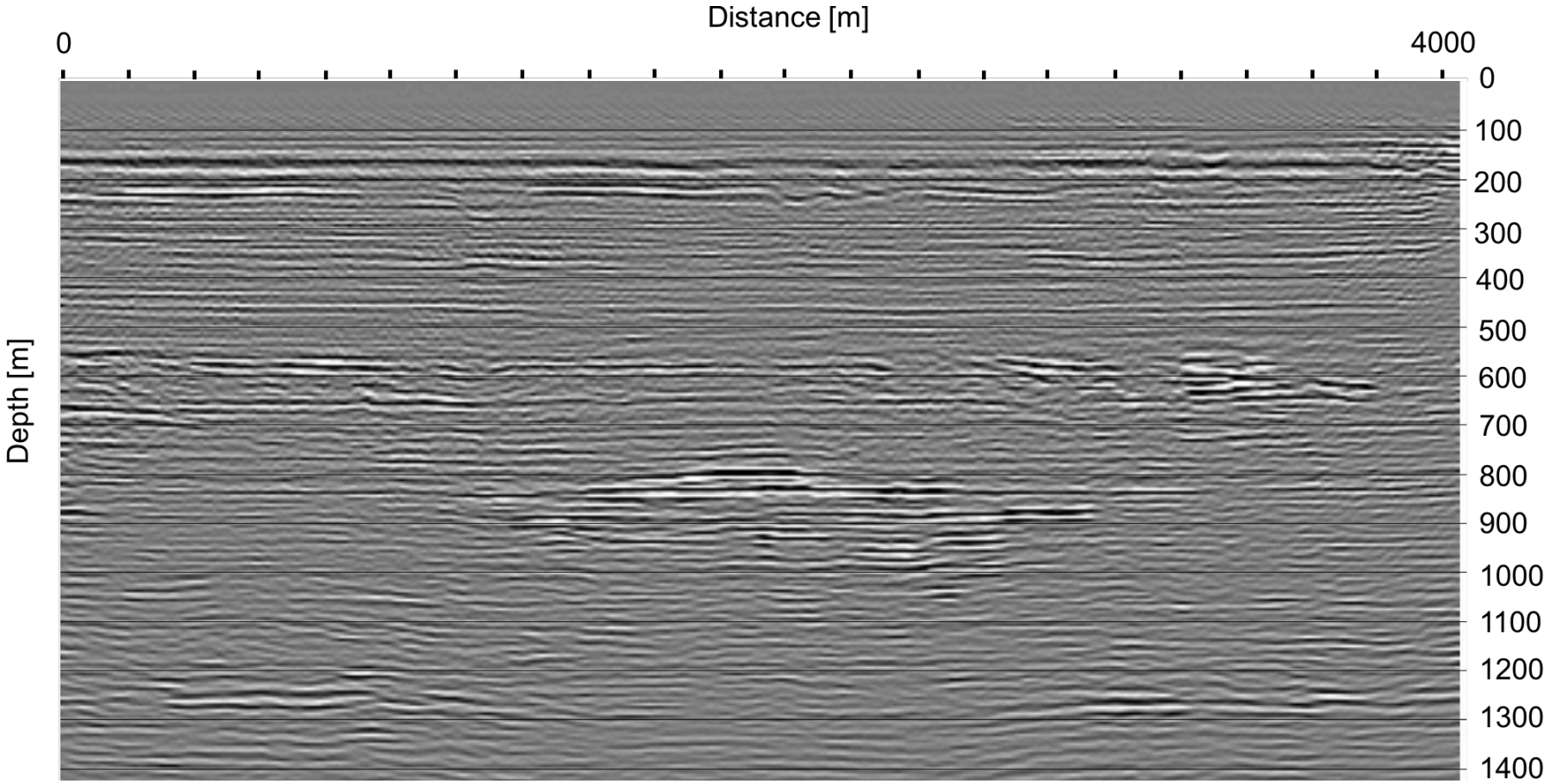

Figure B.5: Seismic image of Angline1. The upper Utsira interface is the negative reflection at a depth of approximately 820 meters.

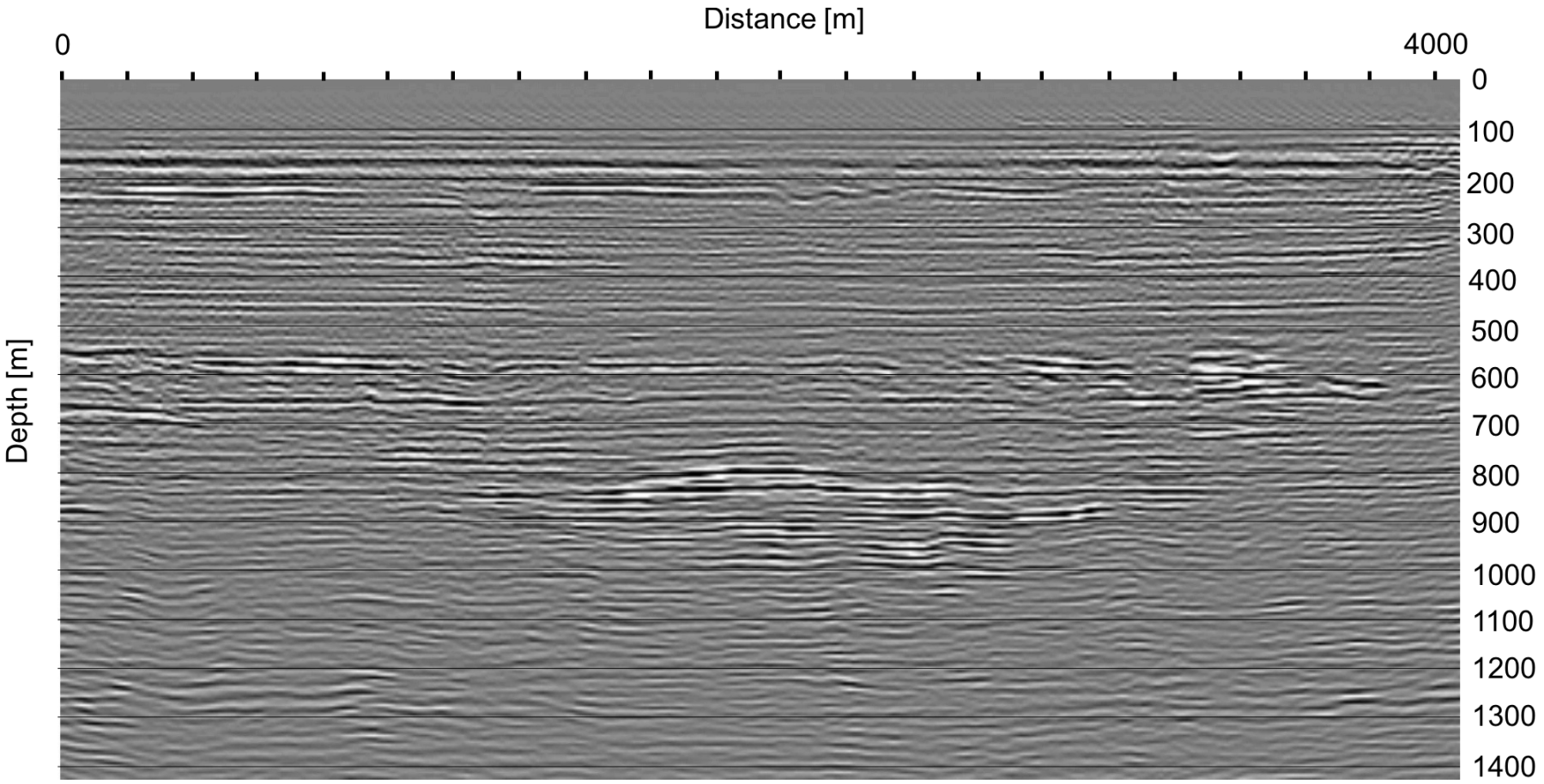

Figure B.6: Seismic image of Angline2. The upper Utsira interface is the negative reflection at a depth of approximately 820 meters.